Development of Advanced High Uranium Density Fuels for Light Water Reactors

Fuel Cycles

James Blanchard
University of Wisconsin, Madison

In collaboration with:
Boise State University

Frank Goldner, Federal POC
Mitch Meyer, Technical POC

NEUP | Nuclear Energy University Programs

U.S. Department of Energy

Final Report

Project Title:	Development of Advanced High Uranium Density Fuels for Light Water Reactors
Covering Period:	October 1, 2011 to November 15, 2015
Date of Report:	February 15, 2016
Recipient:	University of Wisconsin-Madison
Award Number:	11-3041
Principal Investigator:	James Blanchard, University of Wisconsin, blanchard@engr.wisc.edu, 608-263-0391
Co-PIs:	Darryl Butt , Boise State University, darrylbutt@boisestate.edu
	Mitchell Meyer, Idaho National Laboratory, mitchell.meyer@inl.gov
	Peng Xu, Westinghouse Electric Corporation, xup@westinghouse.com
Project Objective:	This work conducts basic materials research (fabrication, radiation resistance, thermal conductivity, and corrosion response) on U_3Si_2 and UN, two high uranium density fuel forms that have a high potential for success as advanced light water reactor (LWR) fuels. The outcome of this proposed work will serve as the basis for the development of advance LWR fuels, and utilization of such fuel forms can lead to the optimization of the fuel performance related plant operating limits such as power density, power ramp rate and cycle length.

Table of Content

1 Executive summary

Uranium nitride

- Phase pure UN fuel pellets with theoretical density of 91.5±1.5% were synthesized via a hydride-dehydride-nitride route. The carbon impurity in the sintered UN was below 2,000 ppm.
- Proton-irradiation of UN-based fuel leads to formation α-U_2N_{3+x} inclusions, which concentration is growing both with the damage level and the irradiation temperature.
- The measured average loop size in UN, α-U_2N_3, and UO_2 is 14.23±3.91 nm, 18.99±4.76 nm and 4.49±1.36 nm, respectively. The measured average loop density in UN, α-U_2N_3, and UO_2 is $(2.54\pm0.40)\times10^{21}$ m^{-3}, $(1.89\pm0.35)\times10^{21}$ m^{-3}, and $(1.70\pm0.15)\times10^{22}$ m^{-3}, respectively. Irradiation damage tolerance of three phases in UN-UO_2 composites follow the sequence of $UO_2 > UN > \alpha$-U_2N_3.
- Under water corrosion tests (250-350 °C, 2400 psi), UN appears to retain its structural integrity slightly better than the UN-UO_2 composites and performs better than as reported in the literature. Increased mass loss occurs with increased corrosion temperature. It is postulated that the UN-UO_2 composites preferentially corrode due to the reaction of UN_{1+X} with the water, resulting in UN_2 and UO_2.
- The thermal conductivity values for as-received and proton-irradiated UN are very scattered and no conclusive temperature effect was observed. The reason for such behavior could lay in the radiation-induced heterogeneity in UN.

Uranium silicide surrogates

- Irradiation promotes accelerated oxide layer growth on Ce_3Si_2 but not on $CeSi_2$.
- As-fabricated Ce_3Si_2 fracture during water corrosion testing. $CeSi_2$ performs better than Ce_3Si_2 from an integrity and oxide thickness standpoint. $CeSi_{1.x}$ shows the thickest oxide layer and formation of silicon dioxide on the surface. The oxide layer formed on all compounds during water corrosion is that of $Ce_{4.67}(SiO_4)_3O$.
- The thermal conductivity values for un-irradiated UO_2, Ce_3Si_2, and U_3Si_2 have a comparable values of about 9 W/(mK), which for proton-irradiated Ce_3Si_2 quickly decays with damage level to half of its value at 0.51 dpa. This result suggests no advantage of U_3Si_2 over UO_2 in terms of initial thermal conductivity or radiation resistance at low temperatures and is caused by the surrogate oxidation. $CeSi_2$, however, shows much higher initial thermal conductivity and better resistance to irradiation.

2   Evaluation of UN fuel

2.1   UN synthesis

The work presented in this section of the report focuses on the synthesis and characterization of UN and UN composite powders and sintered compacts. It should be noted that this work has additionally been communicated through a PhD dissertation, peer reviewed journal publications, and conference presentations (see Publications).

Uranium mononitride (UN) powders were successfully synthesized using two distinct routes that use two different starting materials: the traditional carbothermic reduction of a carbon-uranium dioxide mixture and the hydride-dehydride-nitride of elemental uranium. The carbothermic reduction route is the industrial preferred synthesis route due to the availability and non-reactivity of the starting materials (UO_2 and C) as well as its scalability[1, 2, 3]. However, the primary concern with the carbothermic reduction of UO_2 is the residual carbon and oxygen concentrations of the resulting UN powder, which are critical when assessing corrosion behavior and materials properties of the monolithic forms[1, 4, 5, 6]. Therefore, UN was also synthesized (in parallel) using an atomized elemental uranium starting material where the metal is hydrided, dehydrided, and then nitrided to form UN, as described in the succeeding sections. As can be seen in Figure 1, uranium mononitride has a small phase field and proper processing conditions are critical in the synthesis of high purity uranium mononitride.

Also discussed in this section is the pressing and sintering of UN and UN-UO_2 composites. It is well known that the sintering conditions can drastically alter the microstructure and stoichiometry of the final compact (Figure 1), and therefore the effects of sintering temperature, sintering atmosphere, and composite ratios were investigated. Although the effects of nitrogen concentration in the sintering environment have been shown to affect the final microstructure and stoichiometry of UN and (U,Pu)N in the past,[1, 7, 8, 9, 10] it has not been studied in the fabrication of UN-UO_2 composites.
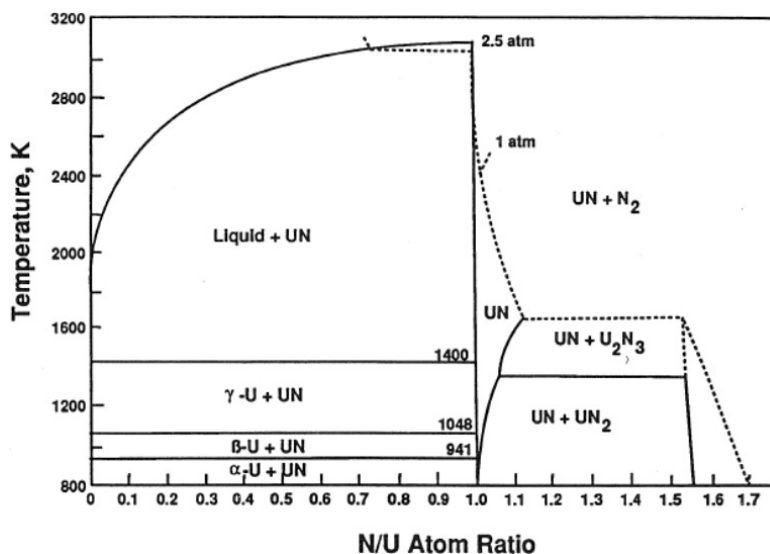
(a)
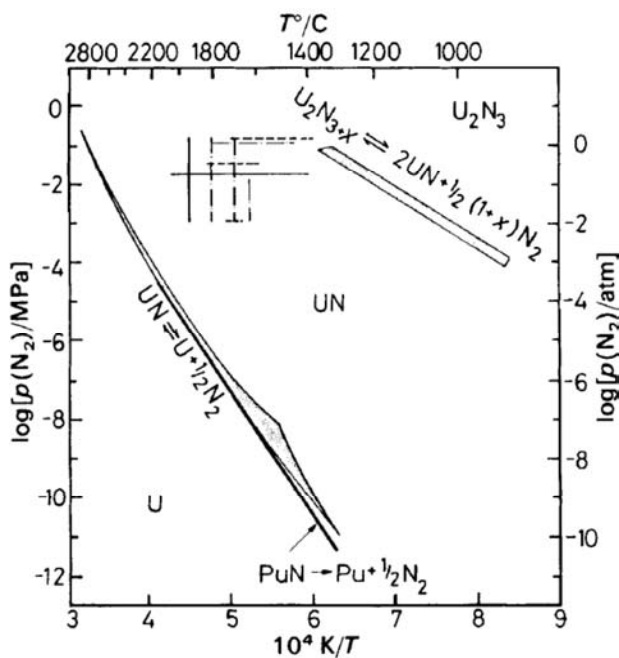
(b)

Figure 1: (a) Phase diagram of the uranium-nitrogen system according to Matthews *et al.*[1] and a plot showing the decomposition pressure of uranium nitrides: U_2N_3 in equilibrium with UN, and UN in equilibrium with nitrogen saturated uranium metal according to Matzke.[9]

2.1.1 *UN Powder Synthesis and Characterization: Carbothermic Reduction*

Multiple variations of the carbothermic reduction of UO_2 + C yielded phase pure UN, as characterized by XRD. UN synthesized by the carbothermic reduction method was done so by mixing a 3.11 or a 2.4 C/UO_2 powder ratio in a milling jar and milling with 50 g of zirconia milling media for several hours. The

UO$_2$ (99.8%, 50 mesh) used was obtained from International Bio-Analytical Industries Incorporated (Boca Raton, FL), which was synthesized from U$_3$O$_8$ via an uranyl acetate dihydrate solution route and has a spherical morphology, as shown in Figure 2. The mixed powders were then placed in an alumina boat and loaded in the furnace for thermal treatment similar to one shown in Figure 3.
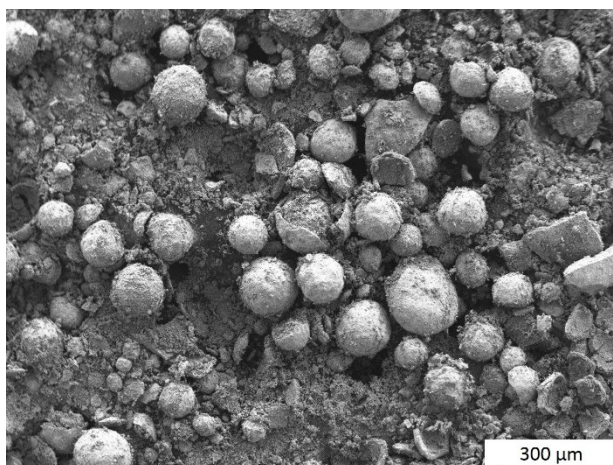

Figure 2: SEM image of the as-received UO$_2$ from Bioanalytical Industries used to mix with carbon powder in the carbothermic reduction prior to nitridation synthesis route to UN.
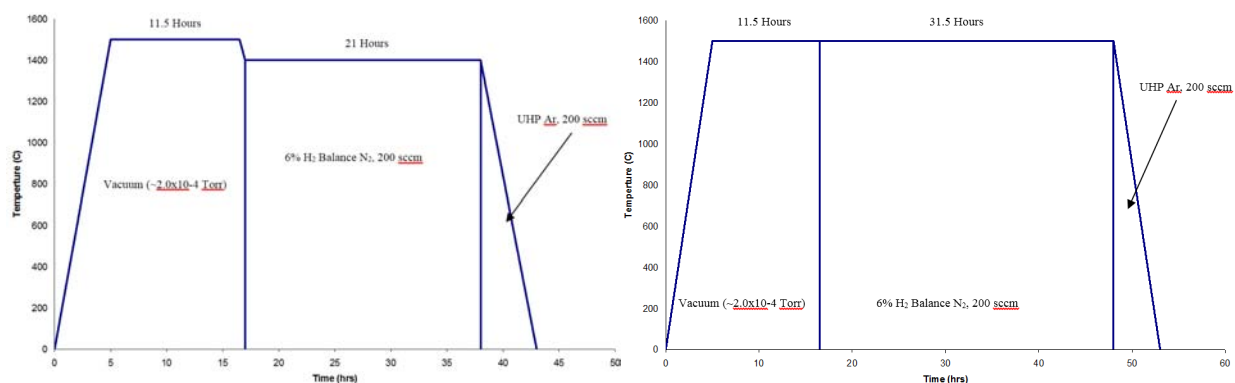

Figure 3: Example thermal profiles used to produce UN via the carbothermic reduction of UO$_2$ prior to nitriding. Temperature profiles and C/UO$_2$ ratios were changed from 3.11 to 2.4 throughout multiple attempts at high purity UN.

Multiple iterations of the carbothermic reduction of UO$_2$ to synthesize UN were successful in producing phase pure UN by changing the dwell times, temperatures, and starting C/UO$_2$ ratios. Carbothermic reduction routes 1-5 used a starting powder composed of a molar ratio of C/UO$_2$ equal to 3.11 and routes 6 and 7 used a molar ratio of 2.4. A select few of the resultant powders were sent for further characterization by LECO chemical analysis at General Atomics. The powder produced using carbothermic reduction route 1 showed significant amounts of residual carbon (approximately 27 at.%) and oxygen (1.1 at.%) in the synthesized UN prompting the iterations. Each of the resultant powders were characterized by SEM and XRD. Figure 4 shows the powder morphology obtained from carbothermic reduction route 1, which used a 3.11 C/UO$_2$ molar ratio. This image is representative of each of the powders resulting from the different carbothermic reduction synthesis routes to UN. Additionally, each of

the powders were characterized for phase using XRD. In each case, the resultant powders were loaded into the stainless steel powder holder were packed, leveled off, and sealed with an x-ray transparent thin film and vacuum grease in the inert prior to diffraction analysis. The x-ray diffraction patterns for all of the powdered samples are shown in Figure 5 below. As it is seen in this figure, most of the carbothermic reduction synthesis routes resulted in a phase pure UN (as indicated by the drop lines and indicators from PDF #032-1397). However, it can be seen that a few of the diffraction patterns show slight variance from stoichiometric UN.
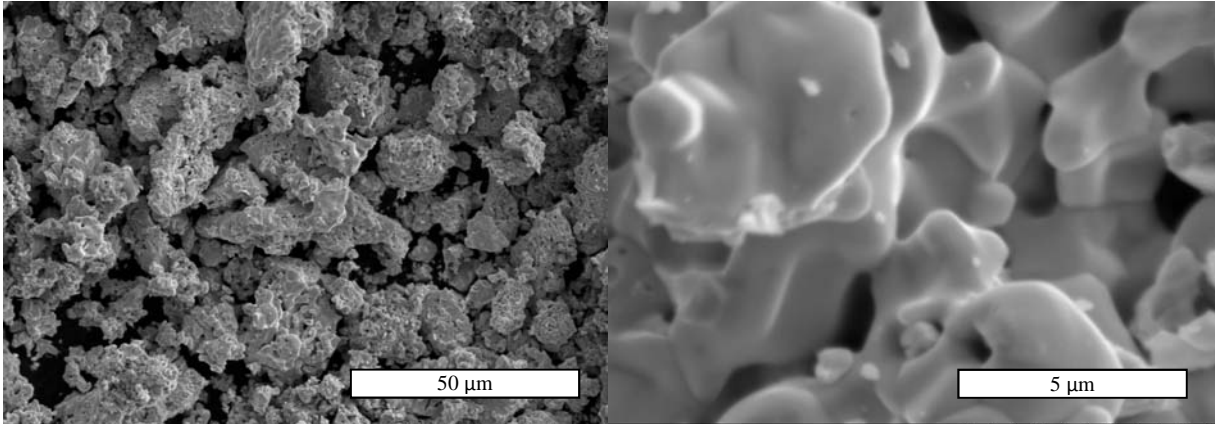

Figure 4: SEM images of the as synthesized UN powder via carbothermic reduction route 1 of UO$_2$ and carbon. The morphology of the powder is typical for each of the carbothermic reduction synthesis route variants.
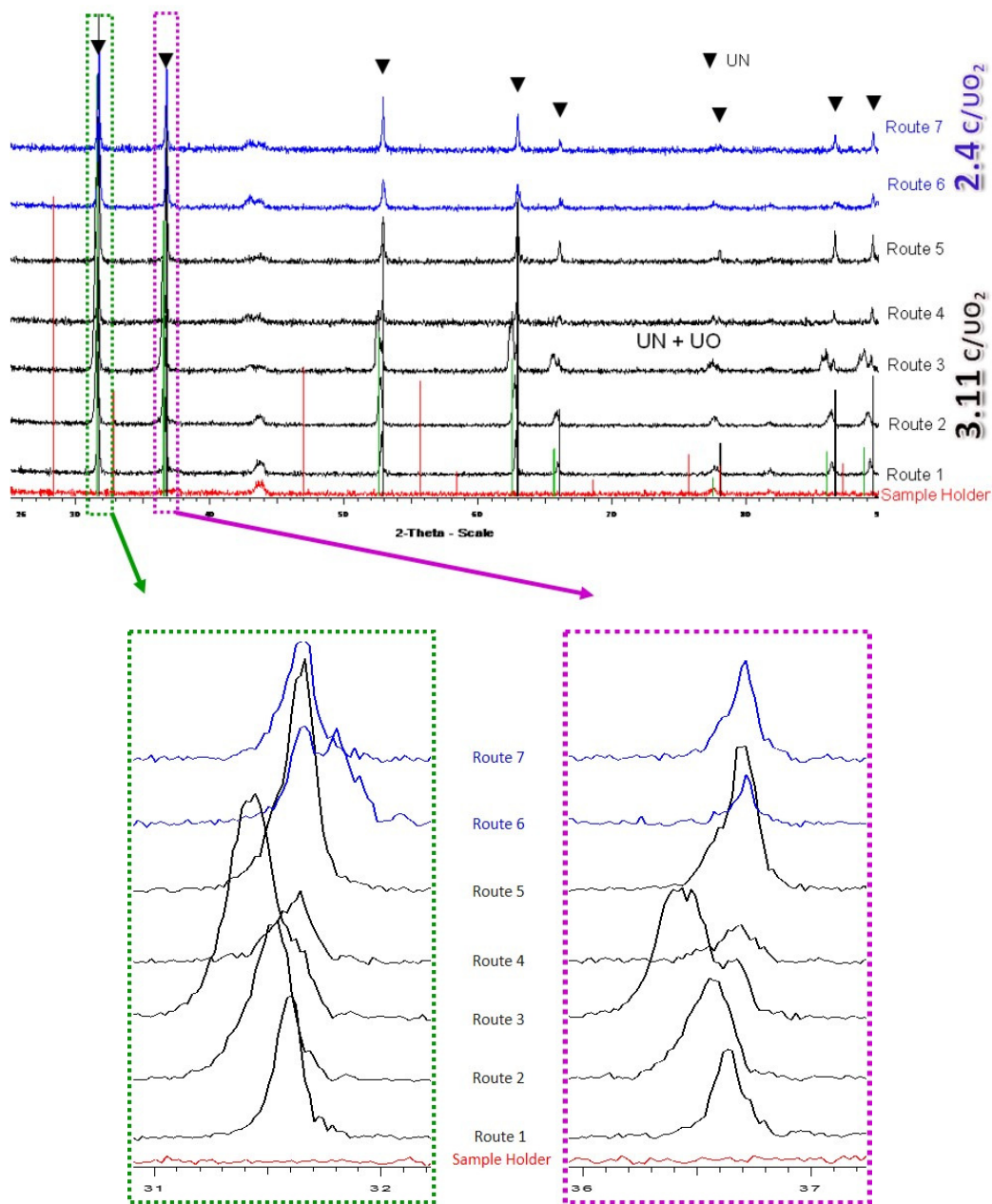
Figure 5: Powder x-ray diffraction on samples produced using various forms of the carbothermic reduction route to uranium mononitride, as previously described. The carbothermic reduction routes using a $C/UO_2 = 3.11$ are shown in black (the lower five) and the routes using a $C/UO_2 = 2.4$ are shown in the top two patterns in blue. The red trace is the result of the stainless steel sample holder.

Assuming that the peaks are only due to UN, the rightward shifts in the diffraction peaks suggest a contraction of the UN lattice (rocksalt structure), which may be explained by vacancy formation. Considering that uranium can have a valence of 6^+, 5^+, 4^+, 3^+, or 2^+, nitrogen can have a valence of 3^- and 2^-, oxygen can have a valence of 2^-, and carbon can have a valence of 4^-, 3^-, or 2^-, many potential defect

mechanisms could occur while maintaining charge balance. The most likely defect models that would cause a shrinkage of the lattice are those that include either cation or anion vacancies. The analysis here includes treating the atomic species (U, O, and C) individually as well as in compounds such as: UO, UO₂, and UO₃. It is assumed that the host lattice is only UN (neither UN₂ nor U₂N₃ are considered), carbon is only in a free state (therefore not including UC, UC₂, nor U₂C₃) and the treatment of U₃O₈ was not included. A few of the vacancy defect models include:

$$3U^{4+} \xrightarrow{UN} V_U''' + \left(3U_{U^{3+}}^{4+}\right)^{\cdots}$$

$$U^{2+}O^{2-} + 3C^{4-} \xrightarrow{UN} \left(3C_{N^{2-}}^{4-}\right)'''''' + O_N^{\cdot} + (2V_N)^{\cdots\cdots} + \left(U_{U^{3+}}^{2+}\right)'$$

$$U^{4+}O_2^{2-} \xrightarrow{UN} (2O_N)^{\cdot\cdot} + (V_U)''' + \left(U_{U^{3+}}^{4+}\right)^{\cdot}$$

$$\left(U^{6+}O_3^{2-}\right) \xrightarrow{UN} (3O_N)^{\cdots} + (2V_U)'''''' + \left(U_{U^{3+}}^{6+}\right)^{\cdots}$$

$$\left(U^{6+}O_3^{2-}\right) + 3C^{3-} \xrightarrow{UN} (3O_N)^{\cdots} + \left(3C_{N^{2-}}^{3-}\right)''' + (V_U)''' + \left(U_{U^{3+}}^{6+}\right)^{\cdots}$$
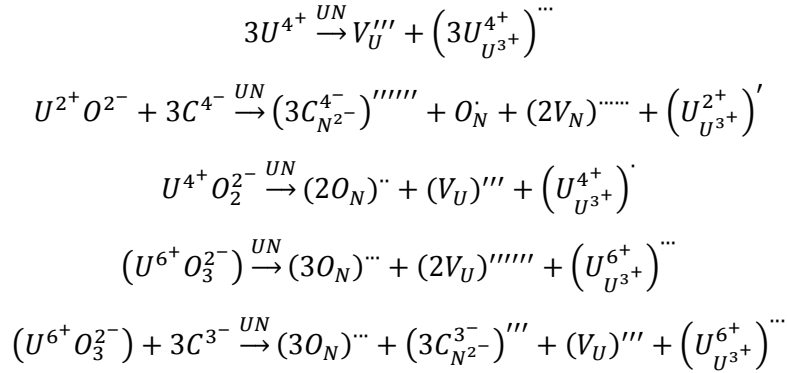
Additionally, there may exist other defect mechanisms which do not include interstitial or vacancy formation but may, or may not, lead to a contraction of the lattice. A few of the substitution defect models include:

$$2\left(U^{4+}O_2^{2-}\right) + 3C^{4-} \xrightarrow{UN} (4O_N)^{\cdots\cdot} + \left(3C_{N^{2-}}^{4-}\right)'''''' + \left(2U_{U^{3+}}^{4+}\right)^{\cdot\cdot}$$

$$\left(U^{4+}O_2^{2-}\right) + 3C^{3-} \xrightarrow{UN} (2O_N)^{\cdot\cdot} + \left(3C_{N^{2-}}^{3-}\right)''' + \left(U_{U^{3+}}^{4+}\right)^{\cdot}$$

$$\left(U^{4+}O_2^{2-}\right) + 3C^{3-} \xrightarrow{UN} (2O_N)^{\cdot\cdot} + \left(3C_{N^{2-}}^{3-}\right)''' + \left(U_{U^{3+}}^{4+}\right)^{\cdot}$$

$$\left(U^{6+}O_3^{2-}\right) + 3C^{4-} \xrightarrow{UN} (3O_N)^{\cdots} + \left(3C_{N^{2-}}^{4-}\right)'''''' + \left(U_{U^{3+}}^{6+}\right)^{\cdots}$$

$$U^{2+} + O^{2-} \xrightarrow{UN} O_N^{\cdot} + \left(U_{U^{3+}}^{2+}\right)'$$

$$2U^{4+} + C^{4-} \xrightarrow{UN} \left(C_{N^{2-}}^{4-}\right)'' + \left(2U_{U^{3+}}^{4+}\right)^{\cdot\cdot}$$

$$U^{4+} + C^{3-} \xrightarrow{UN} \left(C_{N^{2-}}^{3-}\right)' + \left(U_{U^{3+}}^{4+}\right)^{\cdot}$$

$$C^{2-} \xrightarrow{UN} C_{N^{2-}}^{2-}$$
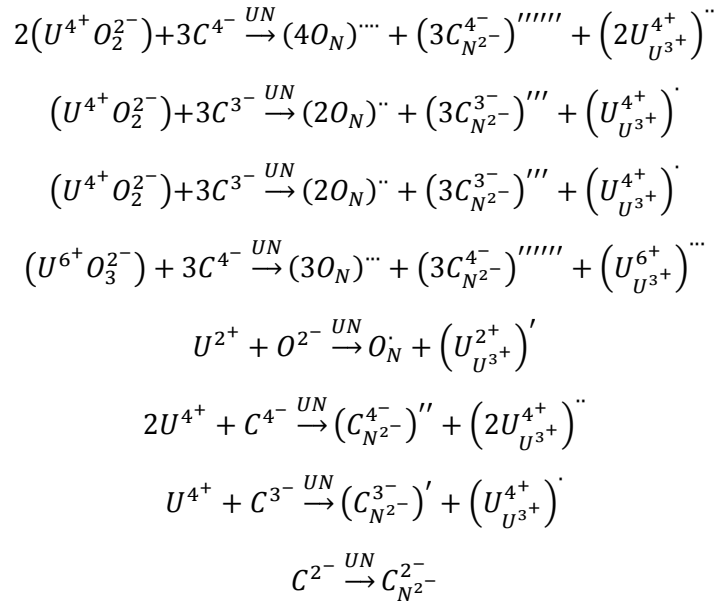
However, since the carbon concentration remained high in each of the powders synthesized using this carbothermic synthesis route, the following process was implemented for providing samples for hydrothermal corrosion studies.

2.1.2   UN Powder Synthesis and Characterization: Hydride-Dehydride-Nitride

As previously stated, in addition to UN synthesis via the carbothermic reduction of UO_2 and carbon, UN was also synthesized via a hydride-dehydride-nitride route. Prior to loading into a tungsten-lined alumina crucible in an argon filled glovebox, the α-uranium (atomized, 99.4%, 50 mesh, received from the Idaho National Laboratories (INL)) shown in the SEM image shown in Figure 6 was cleaned in a 50% nitric acid solution and rinsed in methanol to remove the thin oxide layer. 15 gram batches are loaded into a high temperature alumina tube furnace (CM Furnaces Inc., Bloomfield, NJ, USA), which is immediately vacuum purged to rid the system of any oxygen. The thermal profile used in this work was adapted from a series of previously published techniques[11, 12, 13, 14, 15, 16, 17, 18]. As shown in Figure 7, the reaction was initiated by flowing ultra-high purity (UHP) hydrogen gas (H_2) over the α-uranium while ramping the temperature to 500 °C to "crack" the oxide and form a hydride (Reaction 1). Argon was then introduced to dehydride the powder, as described by Reaction 2 below. The temperature was then reduced to 225 °C and the gas is switched back to UHP-H_2 where the hydrogen uptake is the most rapid[17]. The hydride-dehydride process was completed 2 more times in order to remove as much residual oxygen as possible and provide more surface area for the complete UN reaction. The dehydrided uranium was then subjected to UHP-N_2 and the temperature was ramped to 850 °C where uranium sesquinitride (U_2N_3) is formed according to Reaction 3. In order to reduce the U_2N_3 to UN as in Reaction 4, argon with a reduced nitrogen concentration was introduced and the temperature was briefly raised to 1200 °C before ramping to room temperature. After the nitriding process, the atomized uranium powder (Figure 6, which was a silvery metallic color) became a dark brown-black color and very fine with a high surface area, making the powder very reactive with air.
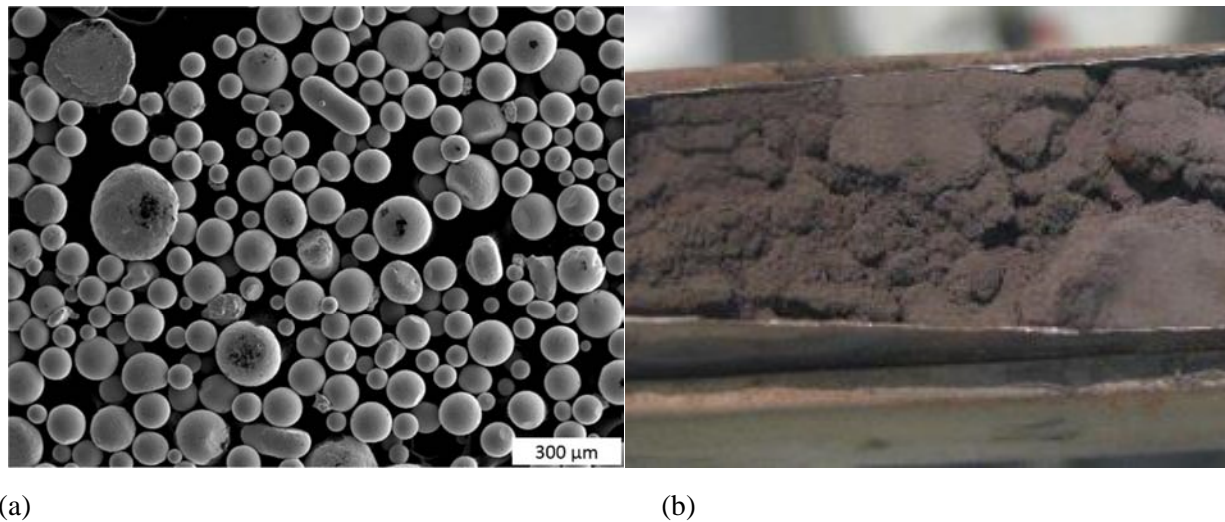

Figure 6: (a) SEM image of the atomized uranium starting materials for UN synthesis via hydriding and dehydriding the metal prior to nitridation and (b) a macro image of the resultant UN powder.

$$U + \frac{3}{2}H_2 \rightarrow UH_3 \qquad\qquad\text{(Rxn. 1)}$$

$$UH_3 + Ar \rightarrow U + \frac{3}{2}H_2 + Ar \qquad\qquad\text{(Rxn. 2)}$$

$$2U + \frac{3}{2}N_2 \rightarrow U_2N_3 \qquad\qquad\text{(Rxn. 3)}$$

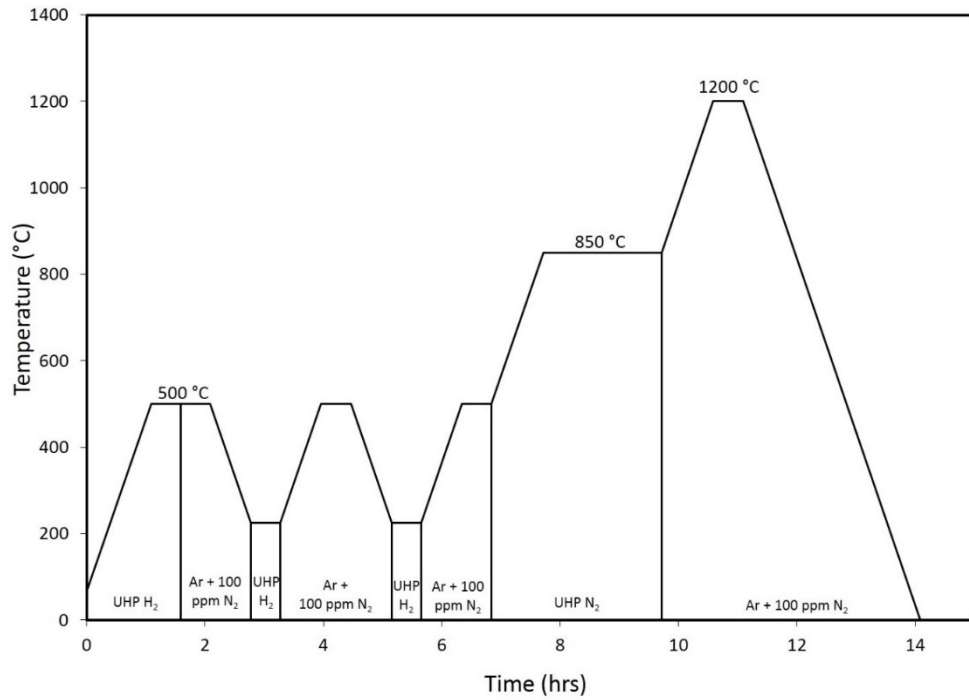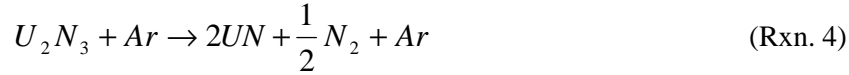$$U_2N_3 + Ar \rightarrow 2UN + \frac{1}{2}N_2 + Ar \qquad\qquad\text{(Rxn. 4)}$$
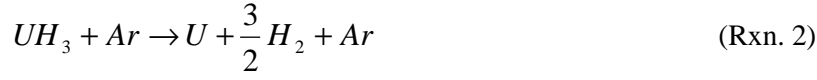

Figure 7: Furnace profile for producing UN from elemental atomized uranium (Figure 6).

Due to the lower residual carbon and oxygen concentrations in the starting material, the hydride and dehydride prior to nitridation synthesis route was the preferred route for fabricating the monolithic pellets. The powder was sent to General Atomics for LECO chemical analysis which suggested that the atomized uranium had 299 ppm and 166 ppm of residual carbon and oxygen, respectively. As seen in Figure 8, the starting uranium was primarily α-uranium with a slight amount of a second phase, which seems irrelevant to the final UN product. Additionally seen in Figure 8, it is seen that the synthesized UN was phase pure according to the ICSD. It should be noted that due to its propensity to rapidly oxidize, the resultant UN was mixed with a vacuum grease to avoid excessive oxidation during the ambient X-ray diffraction (XRD) characterization. Further characterization from LECO chemical analysis suggested that the synthesized powder contained 273 ppm and 2,550 ppm of residual carbon and oxygen, respectively. After synthesis into UN, the powder picked up a significant amount of oxygen but the carbon concentration remained nearly the same. The higher than desired oxygen concentration is likely partially due to the

handling of the highly reactive powder and the fact that the LECO analyzer is not contained within a glovebox, requiring sample exposure prior to weighing and putting in the analyzer. As seen in the SEM images of Figure 9, the as-synthesized UN powder has an irregular morphology and is composed of many agglomerates that are easily broken with milling or mixing to produce a very fine powder.
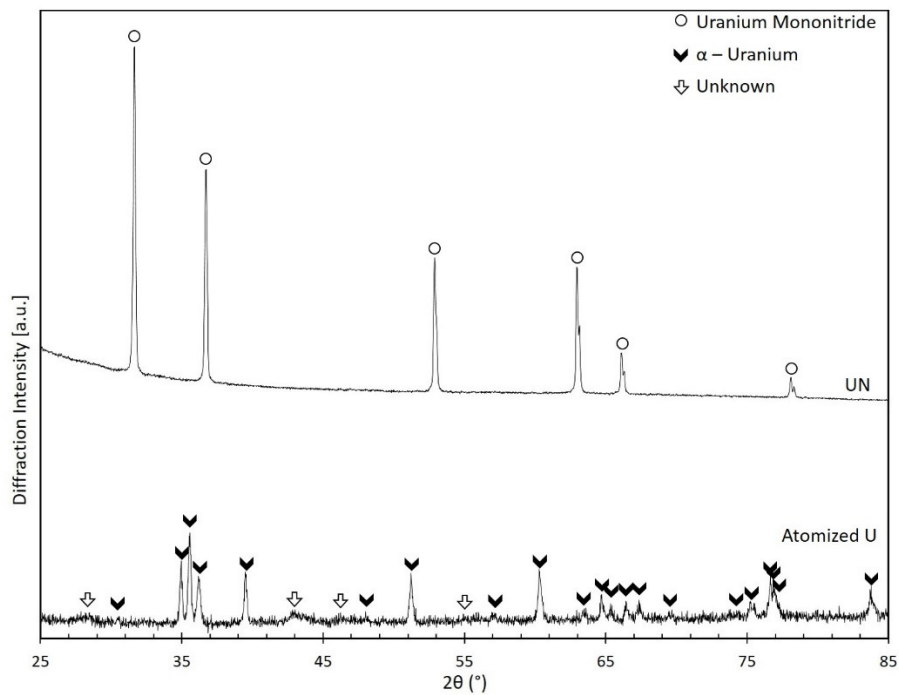

Figure 8: X-ray diffraction pattern of UN powder produced by hydriding and dehydriding atomized elemental uranium prior to nitriding. Further chemical analysis suggests that the powder contained characterization suggests that the powder contained 273 ppm residual carbon and approximately 2,550 ppm residual oxygen.
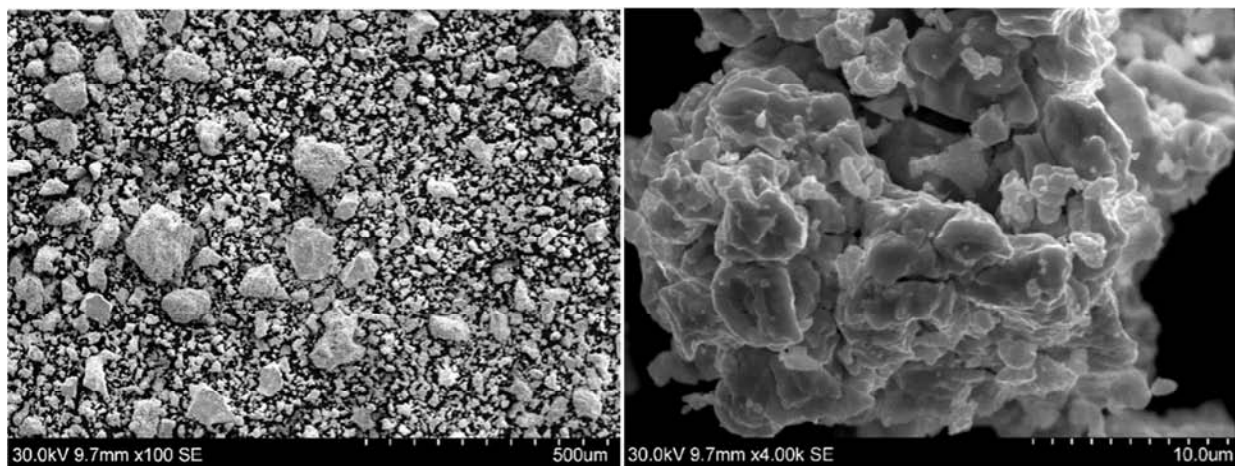

Figure 9: SEM images of the as synthesized UN powder via hydride-dehydride prior to nitridation of elemental uranium.

2.1.3 Consolidation of UN and UN-UO₂ Composites: Pressureless Sintering

Using the UN synthesized from the hydride-dehydride prior to nitridation synthesis route (as described above) and UO_2 (99.8%, 50 mesh, International Bio-Analytical Industries Incorporated), composite powders were fabricated. In the argon backfilled glovebox (maintained with less than 5 ppm oxygen), UN and UO_2 powders were weighed (5 grams with 0, 5, and 10 wt% UO_2) and poured into pre-conditioned polypropylene vials along with 10 mm diameter yttria stabilized zirconia milling media to create a 10:1 media:powder mass ratio. The vials were sealed and transferred to a vertical mixer mill (MTI corporation, 4 tanks mixer) where they were milled for 5 hours at 150 rpm. The resulting powders were characterized using SEM (Figure 10) and XRD (Figure 11). For more detail on this process, refer to the publication by Jaques et al.[19]
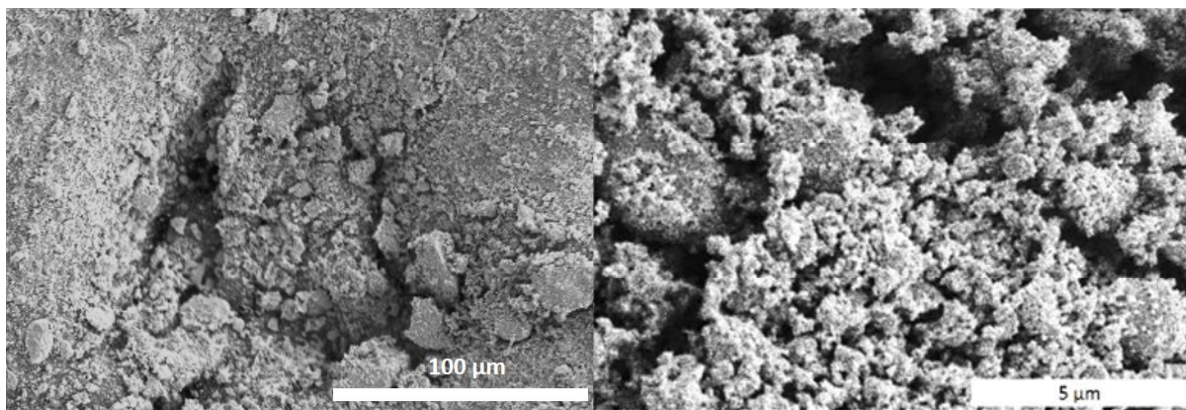

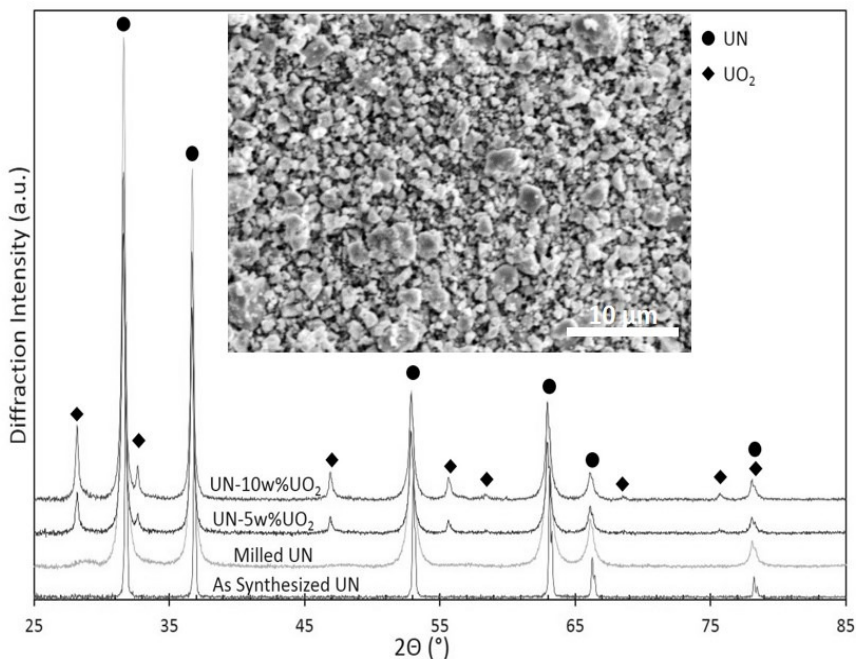Figure 10: SEM images of the ball milled UN powder prior to pressing and sintering.


Figure 11: Powder x-ray diffraction patterns of nominal compositions of UN, UN-5w% UO_2, and UN-10w% UO_2 after milling in a vertical mixer mill for 5 hours at 150 rpm.

Composite pellets of right cylindrical geometry were made using a 3.175 mm pellet die without the use of a binder or lubricant to reduce residual C and O concentrations. The pellets were pressed in an Ar backfilled glovebox at approximately 700 MPa prior to sintering. The green pellets (approximately 62% TD) were placed on a tungsten setter plate and sealed with vacuum grease and a thin PVDC film to prevent excessive oxidation when transferring into the tungsten refractory metal sintering furnace (Thermal Technologies LLC., Santa Rosa, CA, USA). From previous sintering atmosphere studies (0-1 %N_2 in Ar) and sintering temperature studies (1700-2000 °C), the sintering conditions for monolithic pellets were determined as 5 hours at 1900 °C in UHP Ar-100ppm N_2 mixed gas stream. Accordingly, once the pellets were loaded into the furnace, 4 vacuum purge cycles were completed to rid the system of oxygen prior to ramping at 25 $^{°C}/_{min}$ to 1900 °C, where the temperature was held constant for 5 hours prior to ramping back to room temperature at 25 $^{°C}/_{min}$. Once cooled, the pellets were removed and immediately transferred into the Ar glovebox. The densities (determined by an Archimedes technique in water) of the resultant pellets were found to be 91.5 ± 1.5 %TD. The pellets were prepared for SEM and XRD by grinding approximately $^1/_3$ of the material away to create a cross section of the pellets that was perpendicular to the two parallel faces of the right cylinder. The section was polished with 1200 grit silicon carbide. The pellets were fixed to an aluminum sample holder using carbon tape for SEM and EDS characterization (Hitachi S-3400N-II, Japan), as seen in Figure 12. The oxide phase was identified by EDS as the dark intergranular regions in the images. Following SEM, the pellets were fixed to a soda lime glass holder with putty and centered on the XRD (Rigaku, Miniflex 600, The Woodlands, TX, USA) for phase characterization, as shown in Figure 13, which identifies UN and UO_2 phases, according to the ICSD. Additional chemical characterization from LECO analysis is shown in Table 2-1. Two primary conclusions can be drawn from the data in Table 2-1:

1) Most of the oxygen pickup is during UN synthesis

2) the carbon pickup is due from the protective PVDC film (used during sintering) and from milling in a polymer milling vessel. Multiple samples from multiple sintering runs were sent to GA for the sintered pellet analysis.

Table 2-1: A LECO analyzer was used at General Atomics to analyze the light element (carbon and oxygen) concentrations to show trends in oxygen and carbon pickup with processing steps in the UN and UN-UO_2 composite fuel synthesis process.
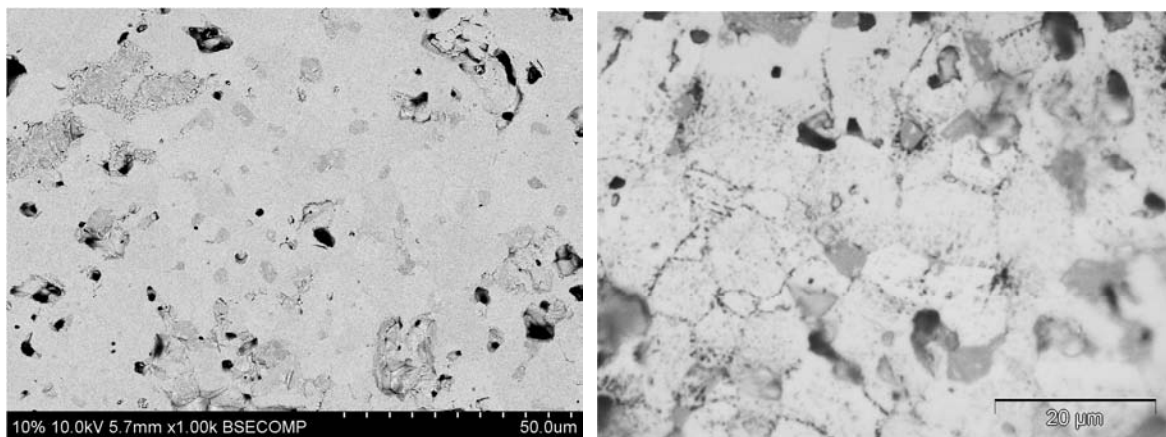
	C (ppm)	O (ppm)
Atomized U	299	166
UN (As Synthesized)	273	2,552
UN (Sintered)	1,964	2,654
UN + 5w%UO_2 (Sintered)	1,812	9,622
UN + 10w%UO_2 (Sintered)	2,378	14,352
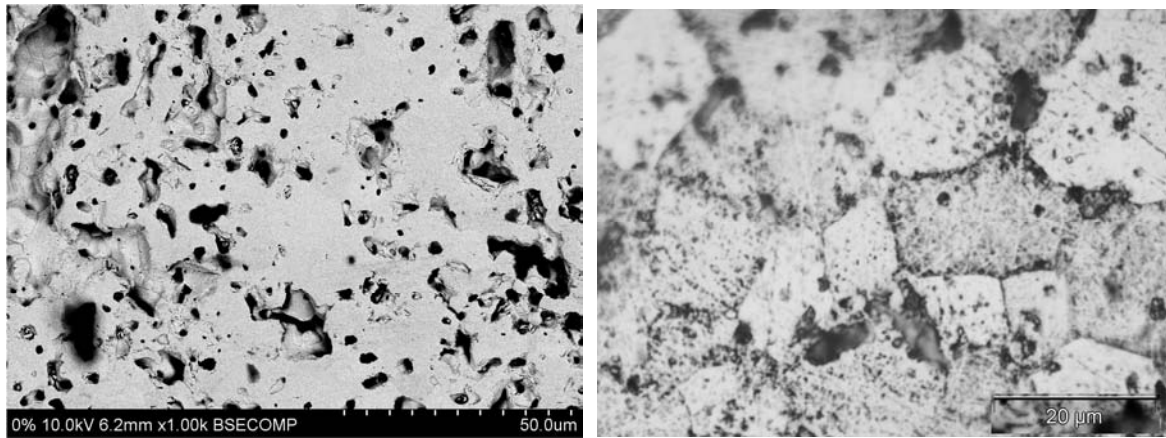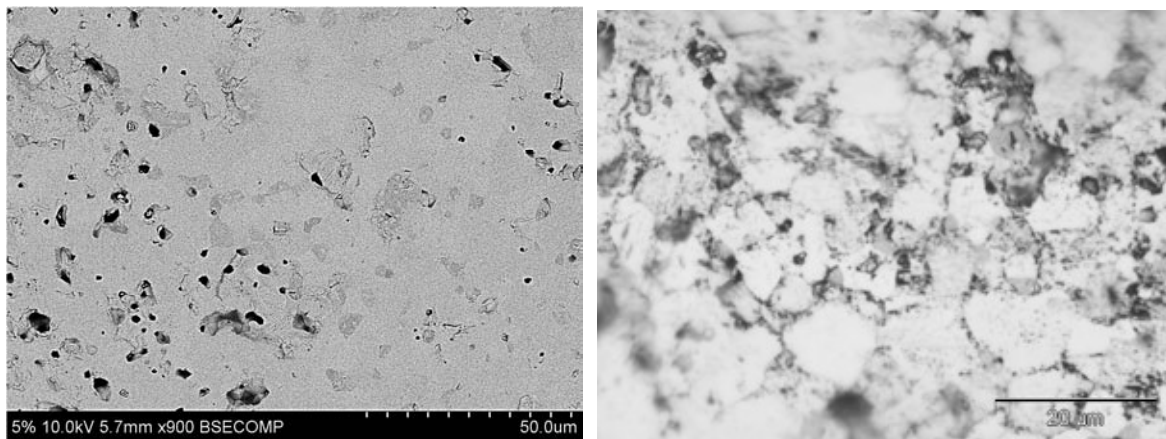
Figure 12: BSE SEM and bright field optical images of the microstructures of (a) UN, (b) UN-5 w% UO$_2$, and (c) UN-10 w% UO$_2$ composite pellets showing the effects of nitrogen concentration on phase formation during sintering for 5 hours at 1900 °C in Ar - 100 ppm N$_2$. EDS confirmed that the dark phase in each of the micrographs is an oxide phase.
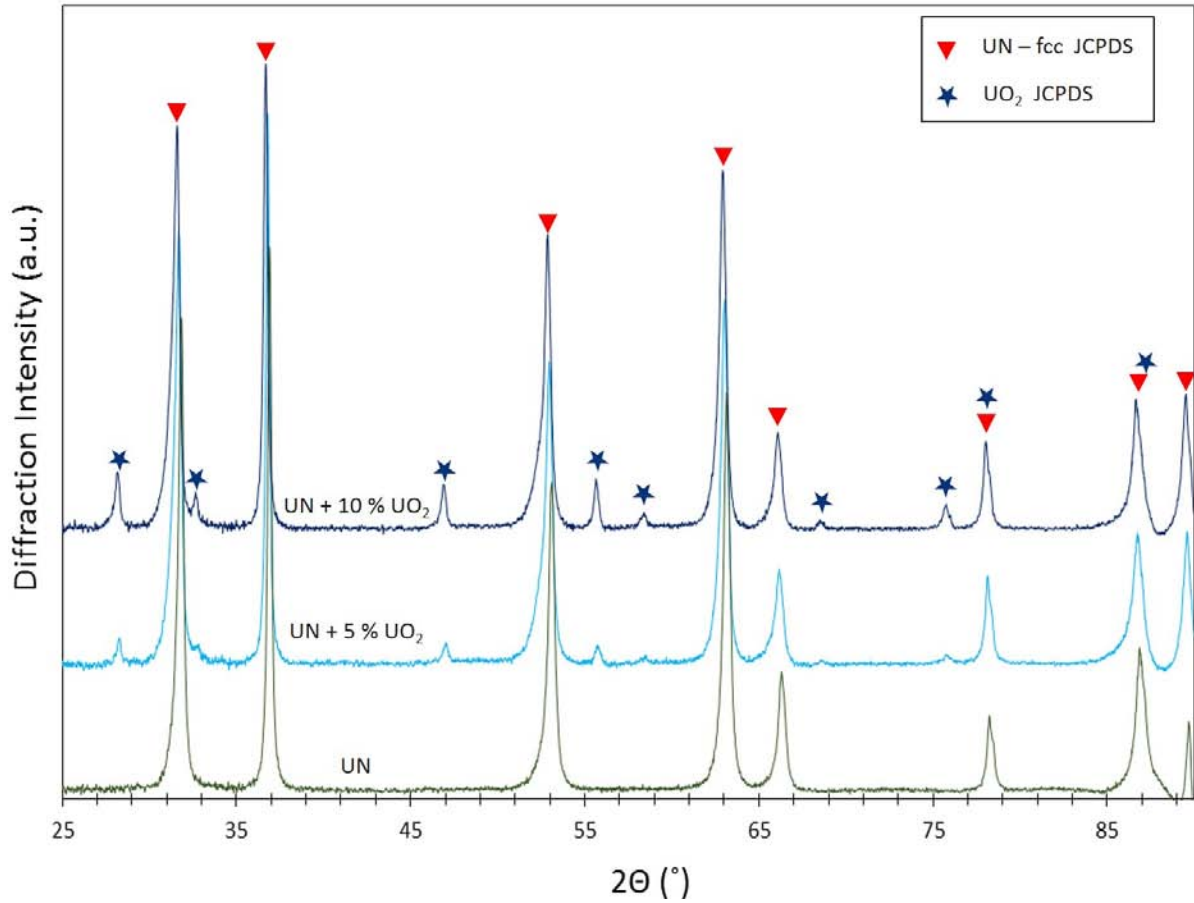
Figure 13: XRD patterns of UN, UN + 5w% UO$_2$, and UN + 10w% UO$_2$ showing phase evolution due to the sintering of the green pellets at 1900 °C for 5 hours in Ar - 100 ppm N$_2$.

2.2   Radiation performance characterization of UN-based composites

12 UN based samples, four from each stoichiometry, were irradiated by 2 MeV protons up to 0.5 dpa and 1 dpa (at 10 µm) at 400 °C (0.22 T$_m$) and 710 °C (0.32 T$_m$). The damage level of 1 dpa corresponds to the fluence of 8×10^{18} p/cm^2. Figure 14 shows the SRIM prediction of the damage depth and ion range for the UN samples calculated using the Kinchin-Pease option with the displacement threshold energies of 40 eV for U and 25 eV for N. The irradiation resulted in the formation of a quasi-flat damage profile with hydrogen interstitials located at the depth beyond 15 µm. The flux was kept around 5.2×10^{13} p/(cm^{2}s) for the lower temperature irradiation and around 7.5×10^{13} p/(cm^{2}s) for the high temperature irradiation resulting in the damage rate between $6.5\text{-}9.4\times10^{-6}$ dpa/s . The samples' temperature was monitored by two thermocouples attached diagonally to the sample holder. Additionally, the uniformity of temperature was controlled by means of IR camera. Both thermocouples maintained a nearly even temperature throughout the experiment. The pressure in the irradiation chamber was better than 10^{-6} Torr.
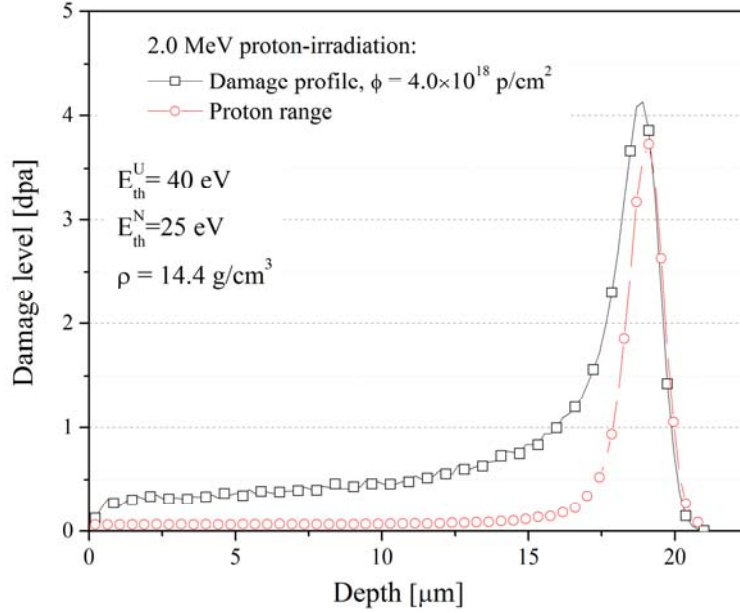
Figure 14: Damage and proton-implantation profile in uranium nitride implanted by 2 MeV protons up to a fluence of 4×10^{18} p/cm^2. Damage level was calculated by SRIM 2013, "Quick calculation of damage" with U-E_{th}=25 eV and N-E_{th}= 15 eV, and theoretical density of 14.4 g/cm^3.

XRD characterization of the damaged UN, UN-5%UO$_2$, and UN-10%UO$_2$ samples was performed to investigate the phase purity after irradiation and lattice constant change (point defect swelling). The XRD analysis of all samples was performed on Bruker D8 Discovery, at 50 kV and 1000 µA, using Cu anode with λ=1.54184 [Å]. 0.3 mm incident slit and 0.3 mm collimator in combination with the Montel mirror and Soller mount were used. The 2D Vantec 500 detector was located 200 mm from the sample. 2θ-θ scans were taken at the range between 22°-70° with 3 steps (600 s/step) starting at 2θ = 30° and increment of 15°. In order to include the maximum number of grains in the XRD analysis, the xy rastering (1 mm by 1 mm, x-speed: 0.1 mm/s, y-speed: 0.2 mm/s) with simultaneous phi rotation (360°, speed 72°/s) was performed. All spectra were striped of K$_{\alpha2}$ line but the background was not removed. Same parameters were used for all investigated samples. The diffraction peaks were identified using the Inorganic Crystal Structure Database (ICSD) [ICSD2015].The X-ray penetration depth was calculated be 1.8 µm, which is much shorter than the thickness of the damage zone.

All reference UN-based samples have inclusions of the U$_2$N$_3$ phase (or UN$_2$) (see Figure 15). Proton-irradiation leads to further formation of those inclusions (see Figure 16) as well as the growth of the UO$_2$ phase in pure UN (see Figure 15) and the concentration of both phases is growing both with the damage level and the irradiation temperature (see Figure 15). The comparison of XRD results obtained from various stoichiometries at the same irradiation conditions (Figure 16) indicates that the growth rate of the U$_2$N$_3$ is comparable in all three materials and dependable only on the irradiation conditions. The analysis of the diffraction rings suggest that the UN phase is in the form of fine grains whereas U$_2$N$_3$ forms bigger grains which act like local single crystals. No measurable peak shift was observed (swelling).
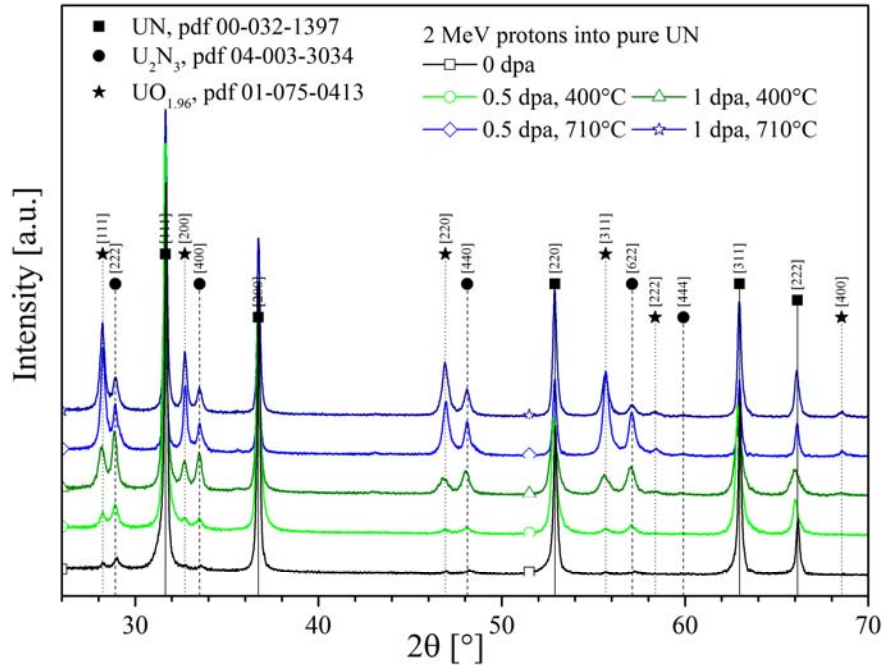
Figure 15: XRD pattern of a UN samples before and after 2 MeV proton-irradiation up to either 0.5 or 1 dpa at either 400 °C or 710 °C. U_2N_3 (or UN_2) and $UO_{1.96}$ phase grow with the irradiation temperature and damage level.
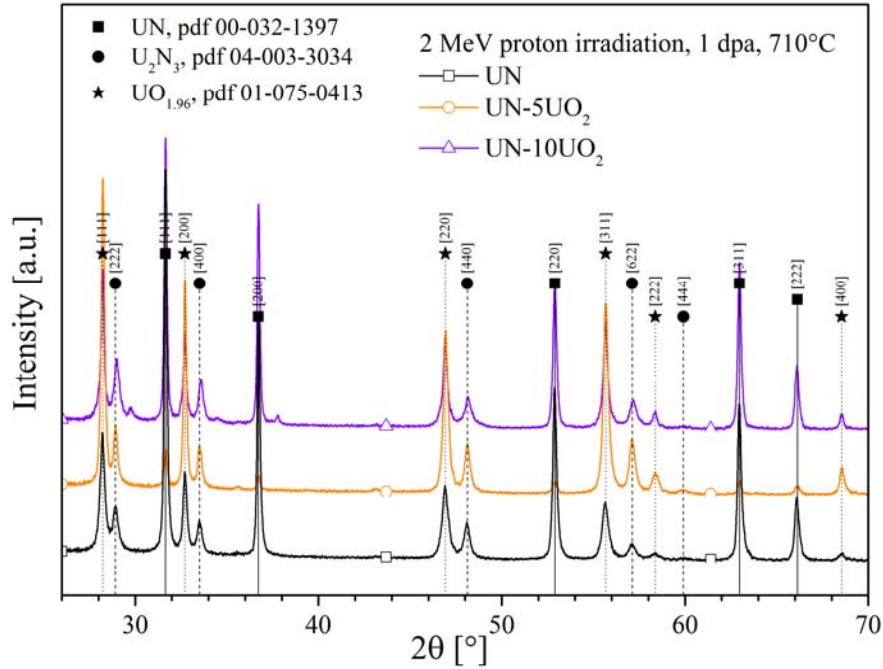

Figure 16: XRD pattern of a UN, UN-5%UO_2, and UN-10%UO_2 samples after 2 MeV proton-irradiation up to 1 dpa at 710 °C.

The microstructure of reference and 2 MeV proton-irradiated UN-5UO$_2$ at either 420 or 710°C up to 0.5 and 1 was analyzed by TEM and STEM. To investigate defect structure in UN-UO$_2$ composite, focused ion beam (FIB) samples were prepared for TEM observation. A lamella was created by coarse trenching 15 µm×10 µm×1 µm sample using the FIB. The sample was then welded to a molybdenum TEM grid for the final FIB thinning. The sample was thinned to a final thickness of roughly 100 nm using 30 keV Ga ions and the final cleaning was conducted using 2 keV Ga ions. The FIB lamella was then characterized with a Tenai TF30-FEG STwin TEM.

The measurements of dislocation loop size and density were conducted manually. Each reported value was the average of 3 measured areas for the number density and loop area per volume measurements and of 200-500 measured features for the size measurements. Statistical errors were calculated from the measurements and are reflected by the error bars in Figure 19. The local foil thickness was measured through inelastic mean free path (IMFP) using electron energy loss spectroscopy (EELS) technique. The IMFP, λ, depends on the specimen density ρ, electron energy E_0 and collection semiangle (excitation semiangle α and collection semiangle β) according to following equations:[20]

$$\lambda = \frac{200FE_0}{11\rho^{0.3}ln\{(\alpha^2 + \beta^2 + 2\theta_E^2 + |\alpha^2 - \beta^2|)/(\alpha^2 + \beta^2 + 2\theta_C^2 + |\alpha^2 - \beta^2|) \times (\theta_C^2/\theta_E^2)\}}$$

where

$$F = \frac{\left(1 + \frac{E_0}{1022}\right)}{\left(1 + \frac{E_0}{511}\right)^2}$$

$$\theta_E = \frac{5.5\rho^{0.3}}{FE_0}$$

$$\theta_C = 20 \text{ mrad}$$

Figure 17 shows the scanning transmission electron microscopy (STEM) image of UN-5UO$_2$ composite after proton irradiation at 710 °C up to a dose of 1 dpa. Large areas of bright phase and gray phase coexist with the small area of dark gray phase. As seen in Figure 17 part of the irradiated UN (about 30% of the damaged zone) material transitioned into α-U$_2$N$_{3+x}$ and UO$_2$ which is consistent with the XRD results. The transition starts at the irradiated surface and proceeds to the bulk. The bright phase, gray phase and dark gray phase are determined as UN, α-U$_2$N$_{3+x}$ and UO$_2$, respectively via selected area electron diffraction (SAED) and electron dispersive spectroscopy (EDS).

Figure 18 shows the dislocation loops in different phases in UN-5UO$_2$ composites after proton irradiation at 710°C and 1 dpa. Figure 19 summarizes the distribution of loop size in UN, α-U$_2$N$_3$, and UO$_2$. The dislocation loops in UN and α -U$_2$N$_3$ are relatively big, while those in UO$_2$ are very small. The measured average loop size in UN, α -U$_2$N$_3$ and UO$_2$ is 14.23±3.91 nm, 18.99±4.76 nm and 4.49±1.36 nm, respectively. The measured average loop density in UN, α-U$_2$N$_3$ and UO$_2$ is (2.54±0.40)×10^{21} m^{-3},

$(1.89\pm0.35)\times10^{21}$ m^{-3}, and $(1.70\pm0.15)\times10^{22}$ m^{-3}, respectively. Assuming all the dislocation loops were formed from the clustering of interstitials into the disk-shaped platelets, the density of interstitials in the loops can be estimated from loop area per volume, S. The calculated S for UN, α -U$_2$N$_3$ and UO$_2$ is 4.04×10^{5} m^{-1}, 5.35×10^{5} m^{-1}, and 2.69×10^{5} m^{-1}, respectively. Based on the loop size and loop area per volume, it is concluded that the irradiation damage tolerance of three phases in UN-UO$_2$ composites follow the sequence of UO$_2$ > UN > α -U$_2$N$_3$.
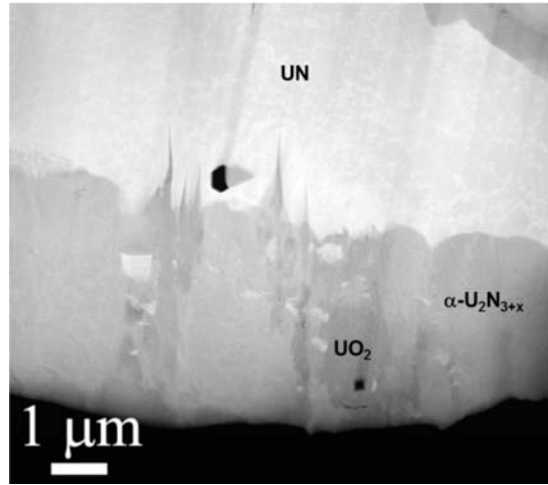

Figure 17: STEM image of UN-5UO$_2$ composite after proton irradiation at 700°C up to a dose of 1 dpa, showing the coexistence of UN, α-U$_2$N$_{3+x}$, and UO$_2$.
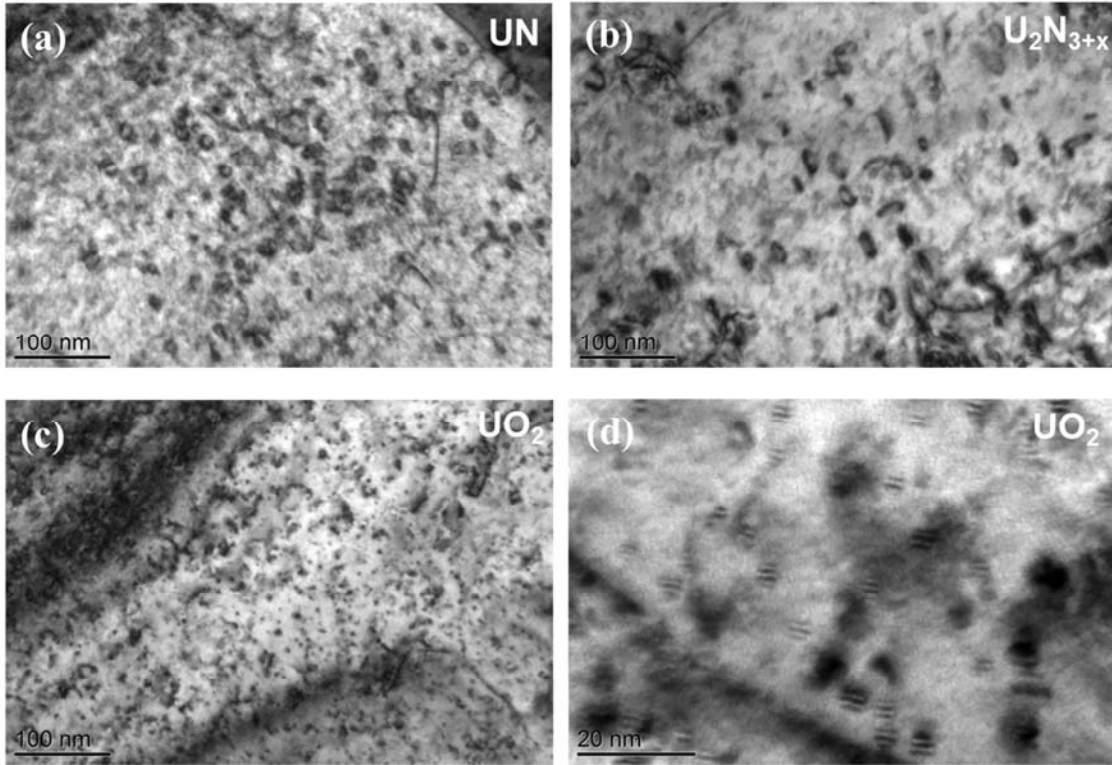
Figure 18: Dislocation loops in (a) UN, (b) α-U_2N_{3+x}, and (c and d) UO_2. (d) is a higher magnification image.
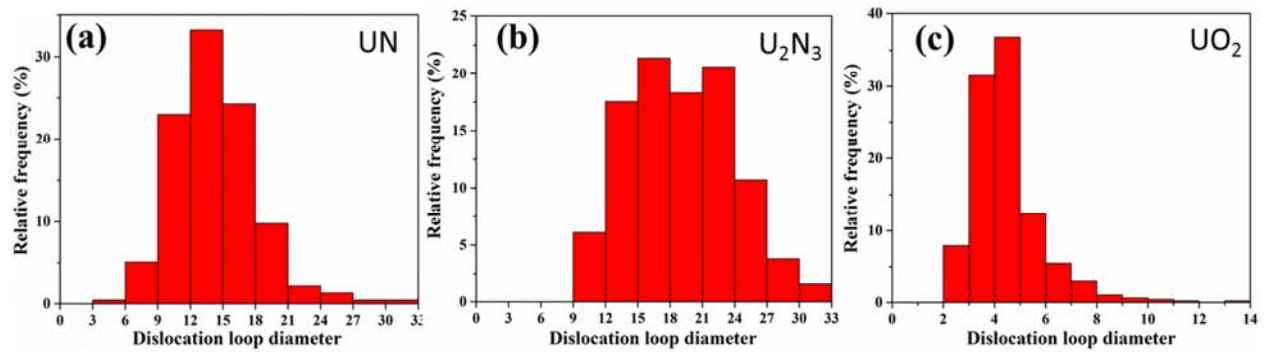

Figure 19: Dislocation loop size distribution in (a) UN, (b) α-U_2N_{3+x}, and (c) UO_2.

The distribution of α-U_2N_{3+x} and UO_2 can be seen again in Figure 20. Both phases exhibit coherent interface and orientation relationship at [001] and [101] zones.
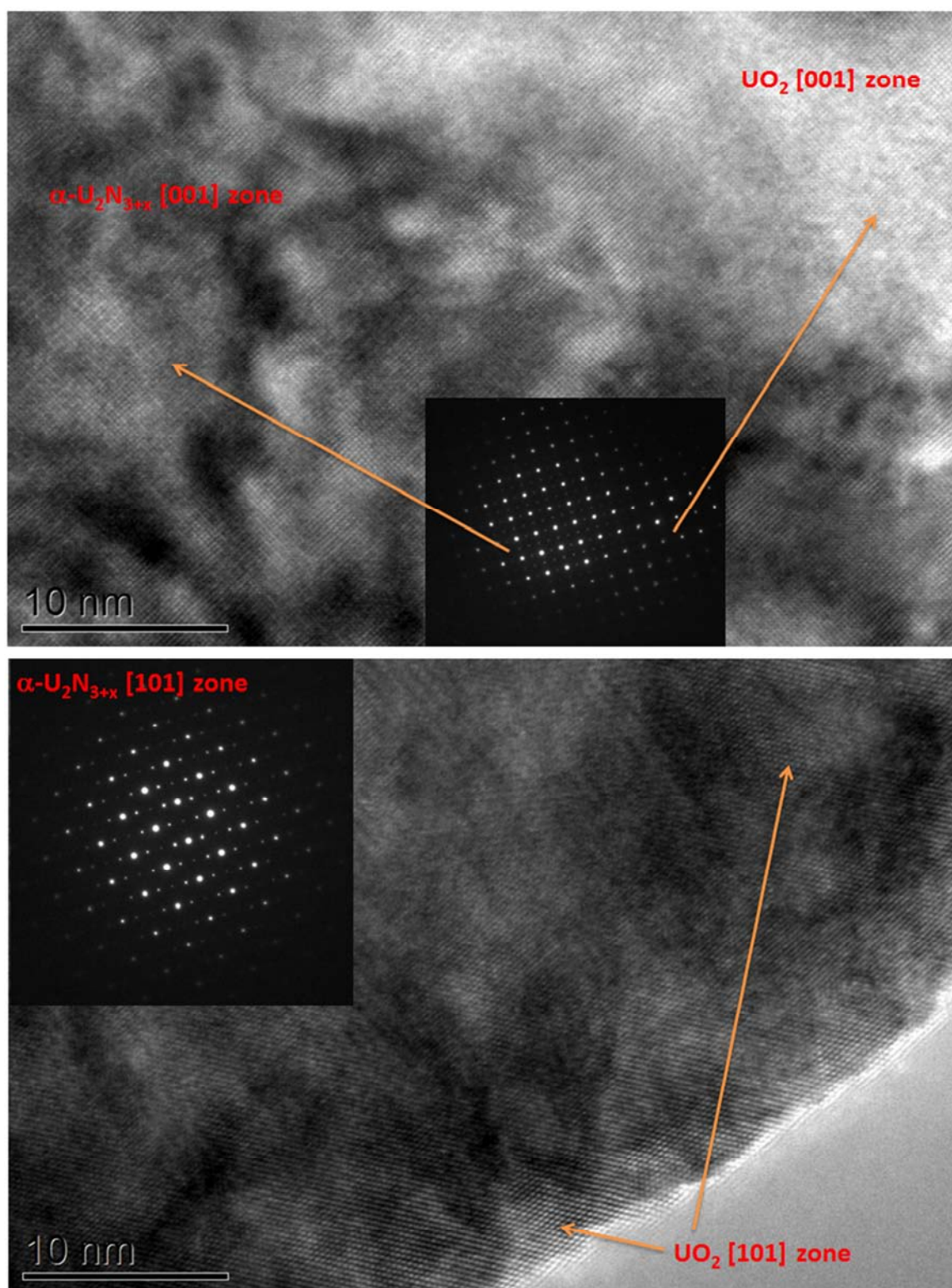
Figure 20: TEM pictures of UN-5UO$_2$ irradiated by 2 MeV protons at 710°C up to 1 dpa.

2.3 UN water corrosion

The work presented in this section of the report focuses on the hydrothermal corrosion of UN and UN-UO_2 fuel compacts. This work has not been published to date, but preliminary data was presented at the Global 2015 conference in Paris, France in September, 2015. Additionally, an abstract titled "Hydrothermal Corrosion Studies on Nitride Fuels" has been submitted to the Top Fuel 2016 conference hosted by the American Nuclear Society. In addition to the conference proceedings, a draft manuscript has begun for submission to the Journal of Nuclear Materials. To this end, more research is planned on the hydrothermal corrosion of UN and UN composites after the completion of this US-DOE-NEUP project using internal funds.

The water corrosion test was performed in Autoclave Engineers Inc. described by Urso.[21] However, modifications to the sample holder and the autoclave were made in order to corrode radioactive samples (depleted uranium). Namely, a custom enclosure was designed and fabricated to encapsulate possible contamination and a stainless steel mesh sample holder was implemented. The autoclave and custom containment enclosure is seen in Figure 21a. The stainless steel mesh sample holder for positioning up to three samples (separated by stainless steel mesh) simultaneously in the hot zone of the autoclave is shown in Figure 21b.
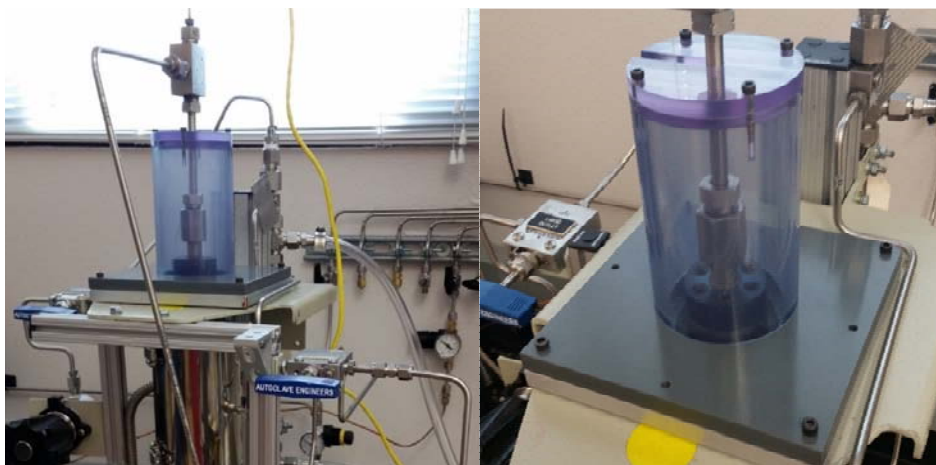
(a)

(b)

Figure 21: (a) Image of the Autoclave Engineers Inc. autoclave with custom fabricated containment enclosure to contain any radioactive materials. (b) Image of the stainless steel mesh sample holder used for positioning up to three samples in the hot zone of the autoclave.

A pellet of each composition was loaded into the sample holder (Figure 21b) in lab air prior to loading into the autoclave along with 80 mL of 18 MΩ de-ionized water. The autoclave was sealed and charged to approximately 4 MPa (600 psi) with ultra-high purity helium prior to ramping the temperature at $1 \, ^{\circ}C/_{min}$ to the dwell temperature, where the temperature (250-350 °C) was held for 30 minutes prior to allowing the pressure vessel to air cool to room temperature. The pressure rises considerably with temperature, to approximately 16.5 MPa (2400 psi) at 350 °C, but the effects of pressure at the corrosion temperature are thought to have little impact on the corrosion behavior of the pellets. It should also be noted that pellets in the 275 °C and 325 °C tests had a diameter of 5.65 mm and a mass of nearly 0.75 gm whereas the rest of the samples had a diameter of 2.8 mm and a mass of nearly 0.2 gm.

Once the pellets were removed from the autoclave, their mass and density was recorded, macro images were taken, and XRD was performed. As seen in the inset of Figure 22, the pellets darkened and the corners of the pellets are preferentially attacked in each case. As expected, increased mass loss occurs with increased corrosion temperature (Figure 22). However, more experiments are planned to replicate the experiments to be able to assess error in the mass loss data. In some cases, indicated in Figure 22, it is seen that no solid mass of pellet was able to be retrieved from the autoclave after corrosion. This material was retrieved as a "sludge" and characterized using XRD in Figure 23d. The trend in corrosion behavior is not yet clear but one important observation to note is that the UN appears to retain its structural integrity slightly better than the UN-UO$_2$ composites and performs better than as reported in the literature.[5, 6, 22] Also, the densities of the pellets (or the remains of the pellets, in some cases) remained nearly constant, at around 90 %TD, as determined from Archimedes measurements in water.
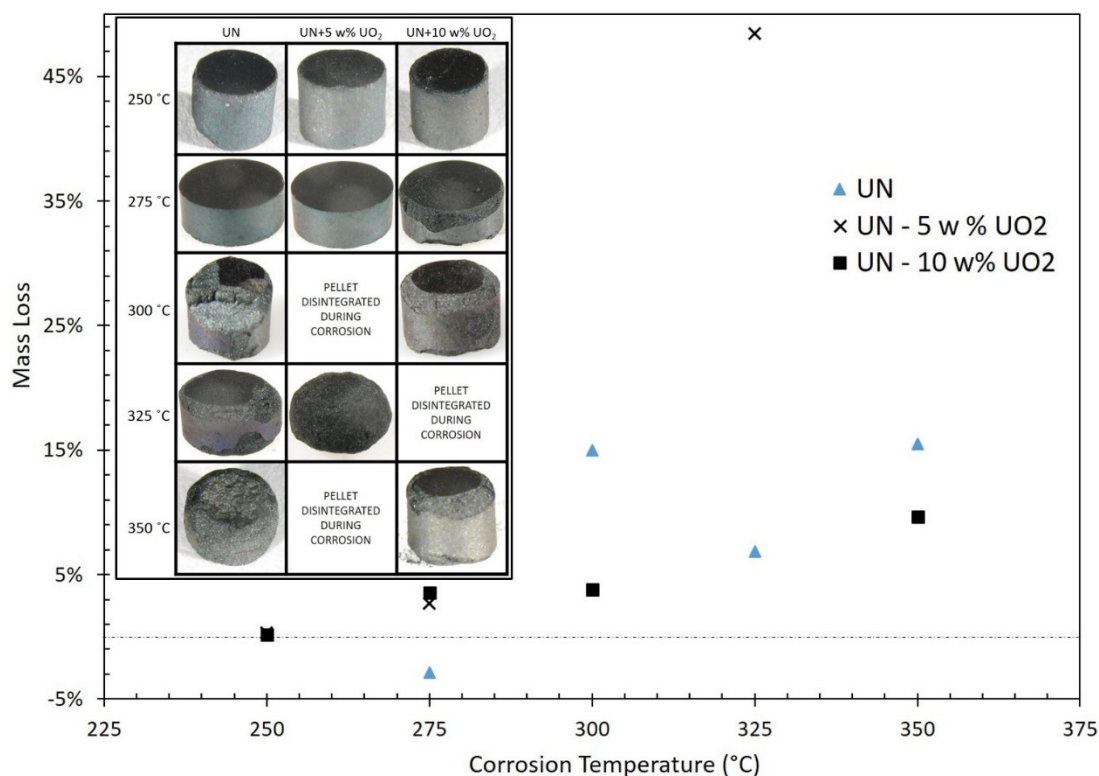
24

Figure 22: Plot showing the mass loss of each pellet after hydrothermal experiment. Macro images of the UN and UN-UO$_2$ composite fuel pellets after hydrothermal corrosion for 30 minutes at the respective temperatures. Note that some UN-UO$_2$ pellets did not survive the corrosion experiments and were retrieved as a "sludge" upon removal of the pellet holder.

XRD of the surfaces of the pellet before and after corrosion is shown in Figure 23 a-c for pure UN pellets, UN-5 w% UO$_2$ and UN-10 w% UO$_2$, respectively. The sludge retrieved from the autoclave was dried and also characterized using XRD, shown in Figure 23d. As noted earlier, the UN pellets out-performed the UN-UO$_2$ composite pellets at higher corrosion temperatures. The primary phase present in the pure UN samples after corrosion is pure UN, excluding the peaks due to the sample holder, but an additional phase becomes prominent in the UN-UO$_2$ composite pellets after corrosion: A hyper-stoichiometric UN phase, UN$_2$. The UN$_2$ phase shows the highest concentration in the surfaces of the pellets corroded at 275 °C, but is also very prominent in the XRD of the sludge, along with the characteristic UN and UO$_2$ peaks. A few more observations made from the XRD are that the UO$_2$ crystallites tend to increase in size when exposed to high temperature water (as determined from the distinct reduction of FWHM of the UO$_2$ diffraction peaks) and the UN$_2$ peaks suggest that the UN$_2$ phase is extremely small and/or exhibits poor crystallinity. It has been shown in previous work that the addition of UO$_2$ results in the formation of a hyper stoichiometric nitride phase[19] during sintering. It is postulated that the UN-UO$_2$ composites preferentially corrode due to the reaction of UN$_{1+X}$ with the water, resulting in UN$_2$ and UO$_2$. However, it is surprising that the pieces left after corrosion remain similar in phase concentration to the pellets prior to sintering, including UN, and the fact that no hydroxide is or other oxide phase are observed. Further work is being completed to validate these preliminary results, better understand the mechanisms of corrosion, and assess the thermodynamics of the UN-UO$_2$-H$_2$O system.
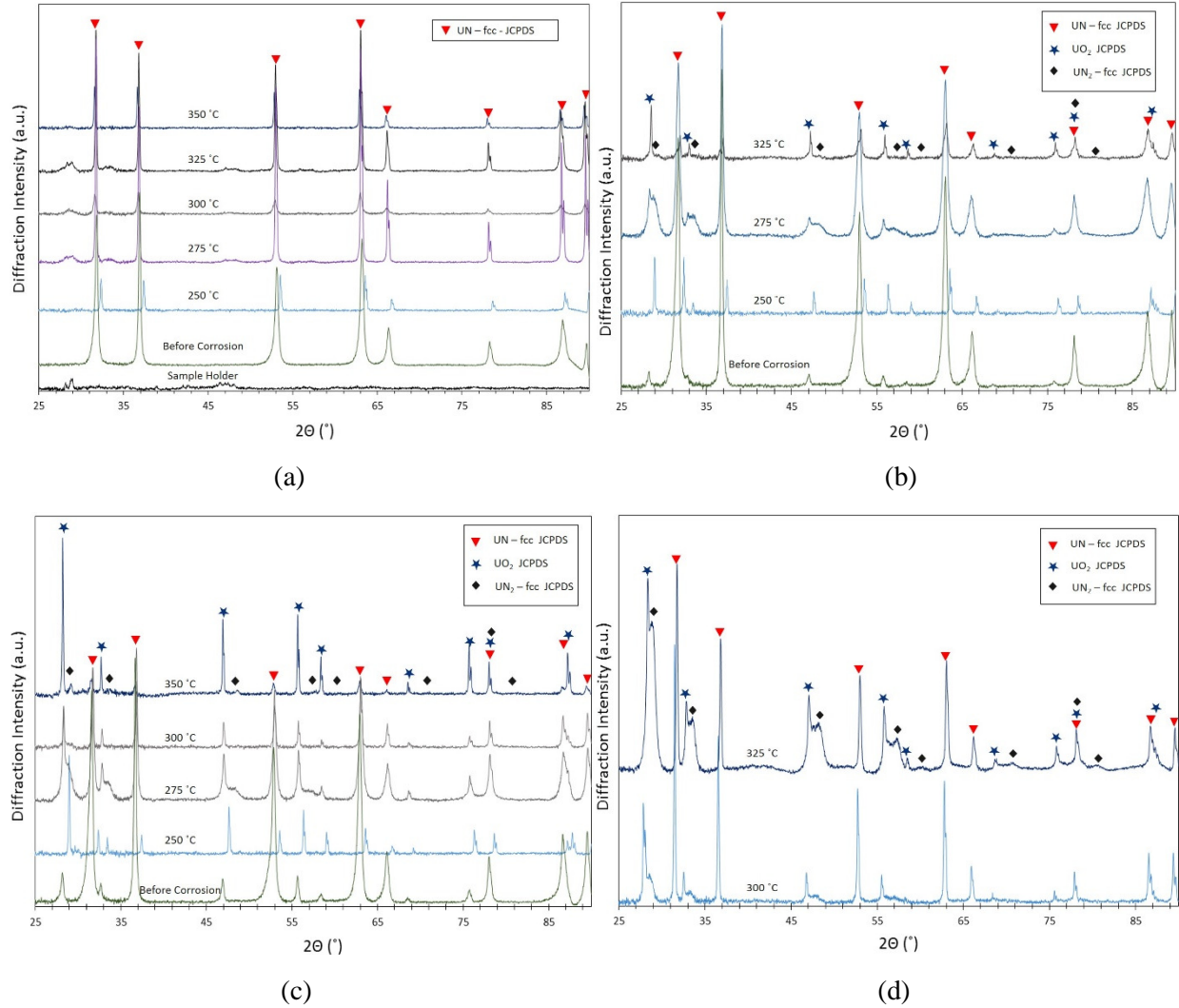
25

Figure 23: XRD analysis of the surfaces of the (a) UN, (b) UN + 5 w% UO₂, and (c) UN + 10 w% UO₂ pellets before and after hydrothermal corrosion at the listed temperatures. XRD of the "sludge" that was recovered from the 300 °C and 325 °C experiments is shown in (d). The background has been subtracted from each pattern.

2.4 Thermal conductivity of UN

Thermal diffusivity D and conductivities λ measurements of as-received and proton-irradiated UN were performed using thermal reflectance measurement techniques in collaboration with the Materials Science and Engineering Department at Idaho National Laboratory.

An initial thin conductive gold coating was applied to all samples to provide high sensitivity for thermal diffusivity. Afterwards, the UN samples we measured for thermal conductivity after a thicker conductive coating was applied to provide high sensitivity for thermal conductivity.

The values of thermal diffusivity measurements were consistent and reproducible during measurement – lower D is observed at lower temperatures due to the presence of dislocations and higher D was measured at higher irradiation temperatures as result of defect recovery. However, the λ values are very scattered

and no conclusive temperature effect was observed. The reason for such behavior could lay in the radiation-induced heterogeneity in UN as reported in Sec. 2.2.

Table 2-2: Summary of the thermal diffusivity and thermal conductivity results.

Sample	Irradiation Conditions	Thermal diffusivity [m^2/s]	Thermal conductivity [W/mK]
UN	Reference	1.44×10^{-6}	2.40
UN	1 dpa, 400 ℃	2.76×10^{-6}	15.10
UN	0.5 dpa, 400 ℃	1.91×10^{-6}	4.94
UN	1 dpa, 710 ℃	3.95×10^{-6}	11.55
UN	0.5 dpa, 710 ℃	2.96×10^{-6}	7.20

3 Evaluation of U$_3$Si$_2$ surrogates

3.1 U$_3$Si$_2$ surrogate synthesis

Cerium sesquisilicide (Ce$_3$Si$_2$) was chosen as a process surrogate for development of a novel, high-energy ball milling route to the synthesis and sintering of uranium sesquisilicide (U$_3$Si$_2$). The work presented in this section of the report has additionally been communicated through a PhD dissertation, 3 master theses, peer reviewed journal publications, and conference presentations (see Publications).

Cerium silicide is one of 10 known isostructural compounds with U$_3$Si$_2$, and the Ce-Si and U-Si phase diagrams are reasonably similar, as seen in Figure 24. While developing a milling and sintering process, minimizing oxygen exposure was identified to be of high importance. Uranium and cerium have similar reactivity with oxygen, and CeO$_2$ is one of only 2 non-radiological isostructural compounds with UO$_2$. These characteristics make Ce$_3$Si$_2$ a good choice for a process surrogate for U$_3$Si$_2$. To briefly summarize this section, phase pure cerium silicide (Ce$_3$Si$_2$) was successfully synthesized using two methods starting with elemental cerium and silicon: high-energy ball milling and arc-melting. The synthesized powders were consolidated using both cold pressing and sintering as well as spark plasma sintering. Initial investigations into the oxidation behavior of the synthesized phases are also presented. The results of the surrogate studies lead to the development of U$_3$Si$_2$ synthesis using similar routes.
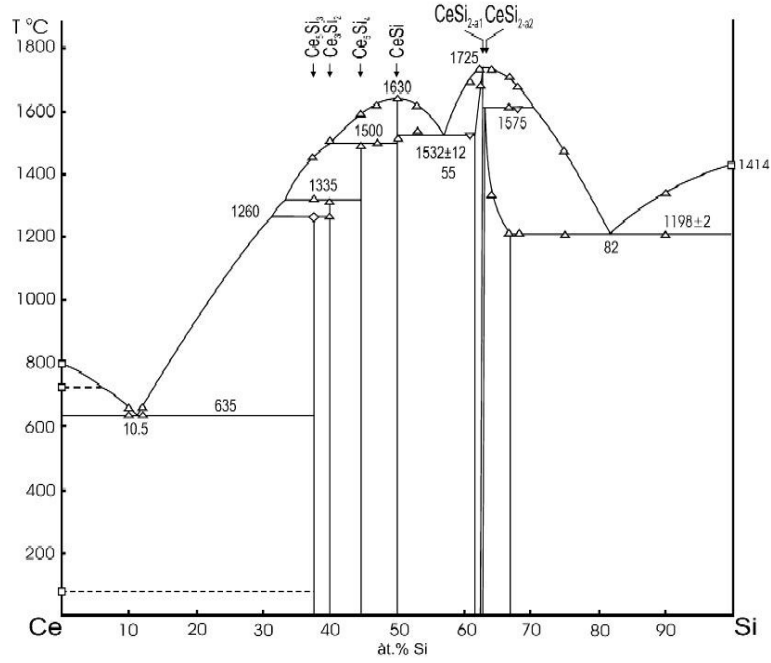
(a)
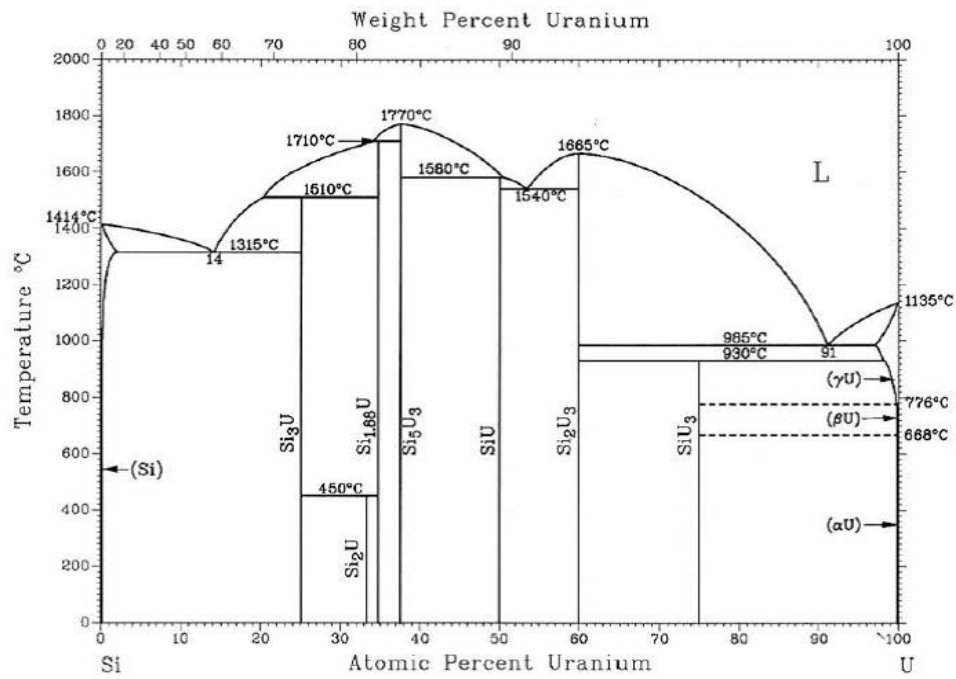
(b)

Figure 24: Phase diagrams of the (a) cerium-silicon system, according to Bulanova *et al.*[23] and (b) of the uranium-silicon system, according to Berche *et al*[24].

3.1.1 U_3Si_2 Surrogate Powder Synthesis and Characterization

In a typical arc melt synthesis, 20.0 gm of elemental cerium (99.999%, -40 mesh, ESPI, USA) was combined with 2.74 gm (2% stoichiometric excess) of elemental silicon (99.9995%, 1-20 μm, Alfa, USA) in an argon glovebox with $P_{O2} < 30$ ppm. The materials were mixed by shaking and pressed into a 35 mm pellet at 67 kN. The pellets tend to crumble slightly at the edges, and future work may require higher pressing load or repressing the pellet. The pellet was loaded onto the copper hearth, placed in a sealed jar, and transported to the arc-melter outside of the glovebox. The hearth was removed from the jar and inserted into the arc-melter under argon flow while minimizing atmosphere exposure to less than 30 seconds. The chamber was purged and refilled with argon 3 times and kept under a slight positive pressure of argon throughout the experiment. Before melting, the atmosphere was purified by striking an arc on a titanium getter material. The initial melt was conducted at 15 A to consolidate the powder into a button and repeated at 30 A after cooling. The button was flipped and re-melted at 30 A 3 times in total. Typical mass loss was 0.5%. To prepare sintered pellets from the arc melted Ce_3Si_2, pea-sized fragments of silicide were ball milled for 15 minutes at 250 rpm in a steel vessel with steel media. The powder thus prepared was extremely fine and pyrophoric.

In a typical ball milling synthesis route, elemental cerium flakes (-40 mesh) were combined with amorphous silicon (~1 μm) in a specific 3:2 molar ratio in an argon atmosphere glovebox ($P_{O2} < 20$ ppm) to reach a total reactant mass of 10 gm. The powders were loaded into a Retsch hardened steel milling vessel (250 mL) with 100 gm of hardened steel milling media (60 gm of 10 mm diameter spheres and 40 gm of 5 mm diameter spheres). It should be noted that in some cases, yttria stabilized zirconia (YSZ) milling media was used and resulted in minor concentrations of detected zirconium. The combination was milled at 500 rpm for 6 hours. After the milling was completed the milling vessel was transferred into the argon glovebox to remove the synthesized silicide. Approximately 30% of the powdered Ce_3Si_2 (3 gm) will be free in the milling jar if starting from a clean jar, while the remainder is cold-welded to the milling jar wall and must be removed by chipping/abrading the adhered material. Yield of free powder may be increased to approximately 80% by milling subsequent syntheses in the same jar without stripping adhered silicide. Process agents such as alcohols and other organic solvents should not be used as they react readily with cerium during milling to produce cerium oxide and cerium silicon carbides. After removing the prepared powder from the milling jar, pass the powder through 250 μm sieve and removed to vials for storage.

In addition to the "typical" processes described above, multiple process variations were also investigated, which included variations in: stoichiometry of starting materials, milling parameters, and other processing conditions. The effects of nominal starting powder stoichiometry is shown in the XRD patterns of resultant powders (Figure 25), where each batch was milled for 6 hr at 500 RPM.
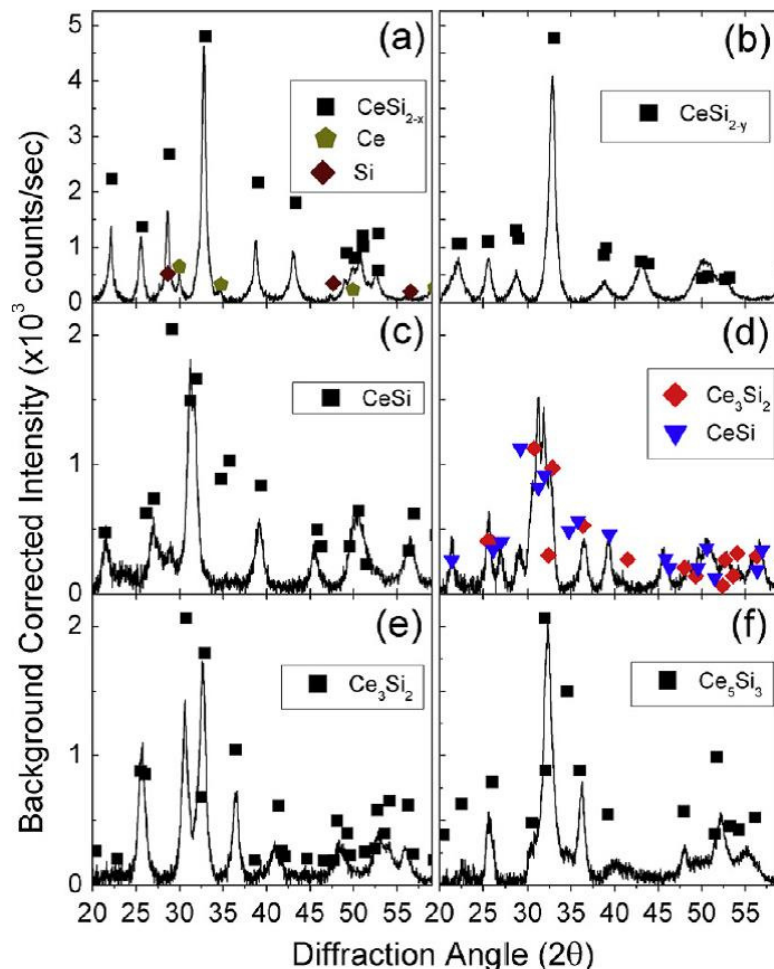
Figure 25: XRD diffraction patterns collected after 6 hr of milling at 500 RPM for the nominal compositions (a) $CeSi_2$, (b) $CeSi_{1.68}$, (c) CeSi, (d) Ce_5Si_4, (e) Ce_3Si_2 and (f) Ce_5Si_3. In each pane, the scatter points indicate expected peak locations as described in each pane's legend. The desired nominal composition phase is indicated in each pane by black squares and was obtained in all cases except Ce_5Si_4 (d), which consisted of CeSi (red diamonds) and Ce_3Si_2 (blue down arrows). The $CeSi_2$ (a) composition contained a slight amount of unreacted Ce (gold pentagons) and Si (maroon diamonds). Adapted from Alanko et al.[25].

In situ temperature and pressure during ball milling synthesis of several nominal silicide stoichiometries ($Ce_3Si_{2\pm x}$ and $CeSi_{2-x}$) was monitored using a Retsch sensing lid (PM GrindControl), which has capabilities of 273 - 473 K, 0 - 500 kPa, and can wirelessly transmit data at 200 Hz to a remote computer. The temperature (measured by a thermistor) and pressure sensors are integrated into recessed locations in the steel sensing lid, which causes some delay in the transmitted temperature values, as described elsewhere.[26] On several samples ($Ce_3Si_{2.1}$, CeSi, $CeSi_{1.9}$), a pressure spike was observed in less than 10 minutes of milling (as seen in Figure 26b). Since all Ce-Si intermetallics have a negative enthalpy of mixing, it is likely that this pressure spike is indicative of a sudden, self-propagating reaction in the milling vessel, termed here as a mechanically-induced self-propagating reaction (MSR). This phenomenon is not observed for compositions of ≤ 40% Si (e.g. Ce_3Si_2 and $Ce_3Si_{1.9}$). To better understand the milling kinetics, a time-resolved study of the nominal Ce_3Si_2 composition was performed. SEM

(Figure 27) was used to better understand the evolution phases (as compared to the Ce-Si phase diagram in Figure 24a) through the milling process.
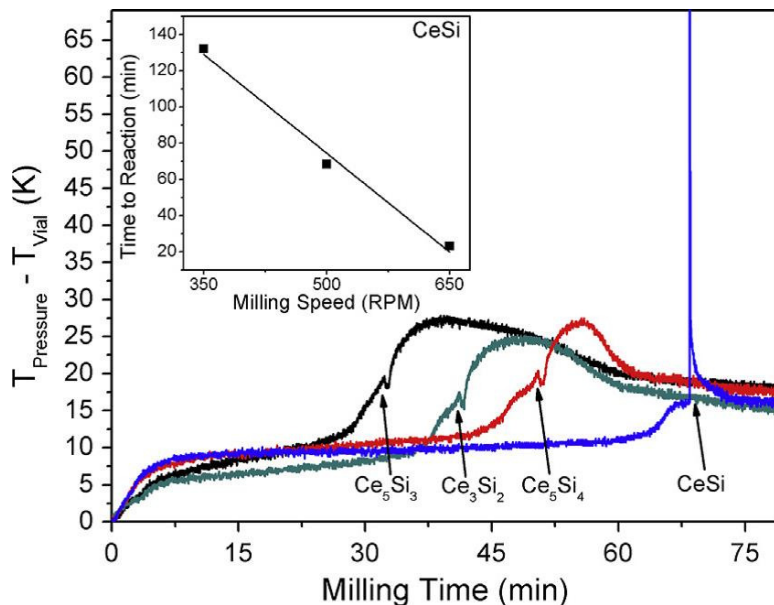
(a)
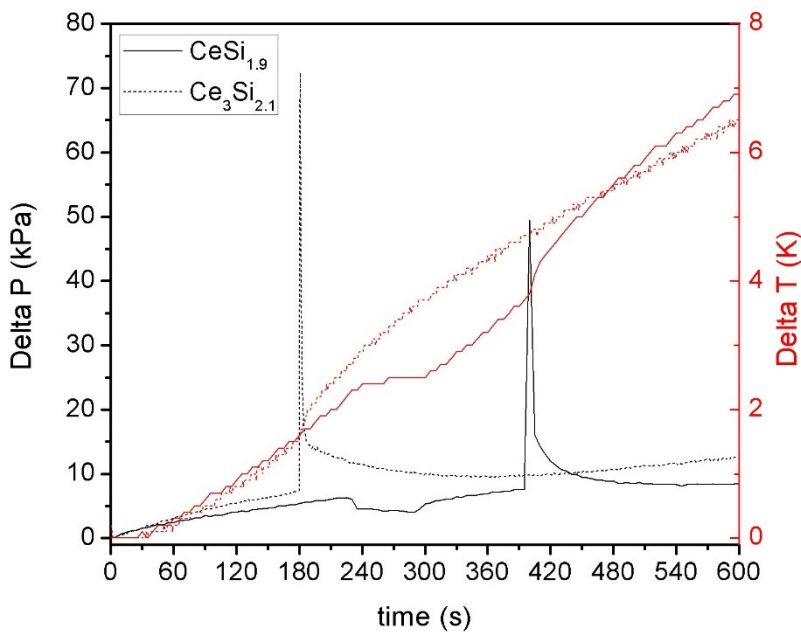
(b)

Figure 26: *In situ* pressure and temperature traces versus milling time from multiple cerium silicides which show pressure and temperature spikes as the materials react. As seen in (a), sharp peaks in the ΔT trace are indicative of a MSR event where the desired phases are formed (adapted from Alanko *et al.*[25]. The zoomed in data (b) show significant pressure spikes with a corresponding (small) rise in temperature which is also indicative of an MSR event. (The plateau in the CeSi$_{1.9}$ data is due to turning off the mill briefly to retighten the retaining bolts on the lid clamp).
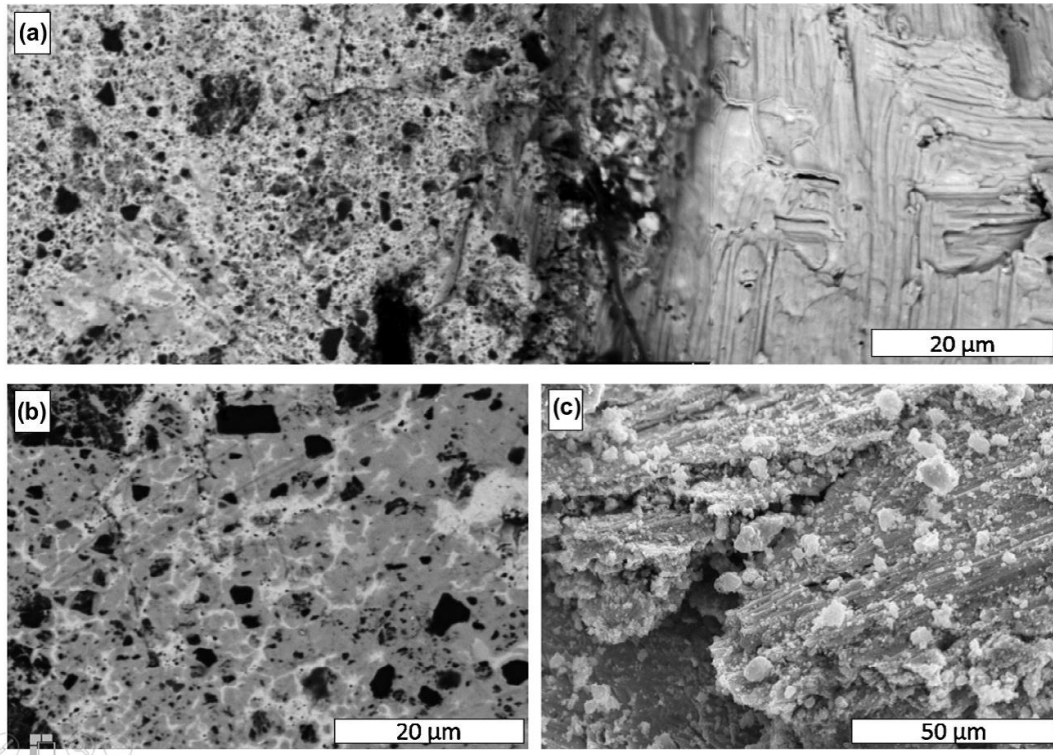
Figure 27: SEM micrographs of nominal Ce_3Si_2 powder just before (c) and after (a, b) the MSR event observed in Figure 26. The BSE image of a sectioned and polished fragment immediately after the MSR event (a) shows an inhomogeneous interior (left side of image) encased in a smooth cerium exterior (on the right) which implies that melting occurred during the reaction. Another area of the sample in (a) shows a three phase region (cerium, Ce_2Si_3, and silicon). The SE image in (c) shows that the before the MSR event, silicon particles are layered with cerium sheets. Adapted from Alanko, *et al.*[25].

After 1 hour of milling, the free powder collected from the milling jar had somewhat spherical morphology and fairly regular particle size distribution between 10-50 μm, as seen in Figure 28. The particle size is observed to decrease with increased milling time, but this relationship was deemed relatively unimportant to the current goals of the project and was not pursued further.
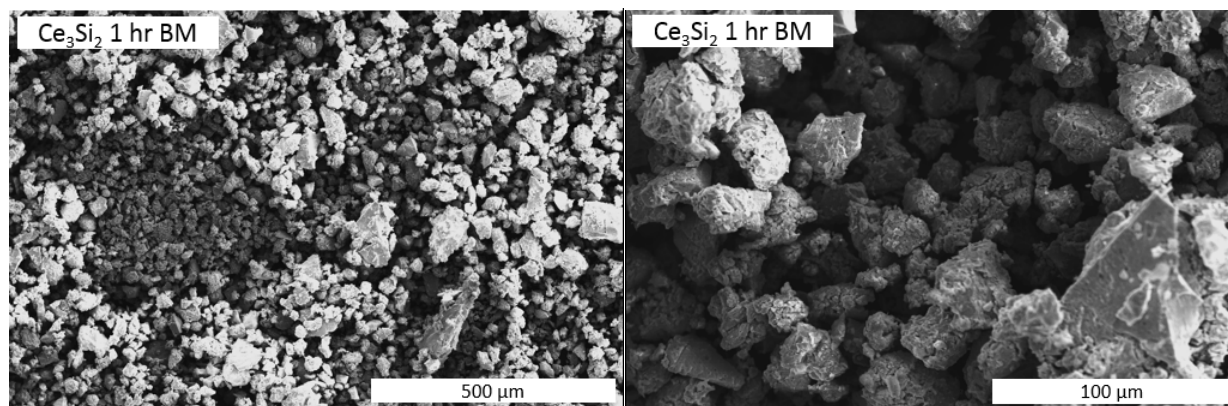
Figure 28: The SEM micrographs show the particle morphology of the synthesized Ce$_3$Si$_2$ after ball milling for one hour.

3.1.2 *Consolidation of U$_3$Si$_2$ Surrogates: Pressureless Sintering (PS)*

The previous section discusses synthesis routes to the formation of a U$_3$Si$_2$ surrogate, Ce$_3$Si$_2$, whereas this section discusses the consolidation of monolithic samples using traditional pressureless sintering (PS) techniques as well as a more novel approach; spark plasma sintering (SPS). Samples for PS were prepared in an argon filled glovebox that was maintained at around 20 ppm oxygen. Approximately 1.5 grams of powder (sieved through a 250 μm sieve) was used for each pellet. The powders were poured into a 13 mm (inner diameter) steel die and cold pressed. The press was held for 1 minute at 67 kN then slowly bled off to 45 kN and 22.5 kN with a 1 minute hold at each pressure. Green pellets were weighed and loaded into an alumina boat lined with niobium foil before transferred to a high temperature alumina tube furnace in a glove-bag with flowing argon. Immediately after loading, the furnace was evacuated to $4*10^{-4}$ Torr and backfilled with UHP argon passed through an oxygen scrubber to reduce the oxygen levels to less than 1 ppb. During sintering, the temperature was raised at 150 $^{\circ}C/_{hr}$ to the desired dwell temperature where it was held for 12 hr. The pellets were then cooled to room temperature at a rate of 150 $^{\circ}C/_{hr}$. These pellets were free of an oxide phase and essentially phase pure by XRD (Figure 29).
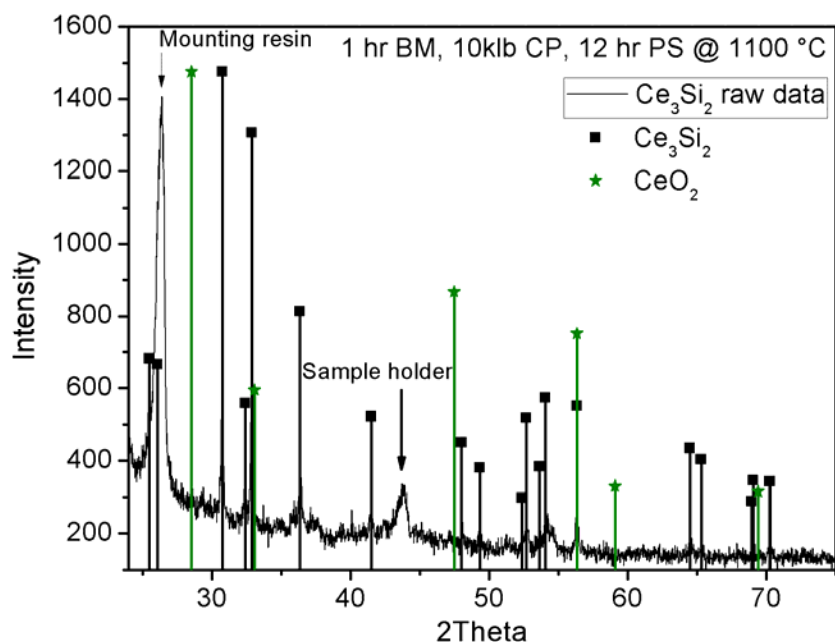
Figure 29: X-ray diffractogram of a monolithic Ce_3Si_2 pellet pressureless sintered at 1100 °C. The droplines sown are the expected peak locations for the desired Ce_3Si_2 (black squares) and cerium oxide (CeO_2, green stars).

The Ce_3Si_2 SEM data suggest a small grain size as shown by the fracture surface SEM image in Figure 30. In this figure, there is a dark area which is shown by EDS to have high levels of carbon (Table 3-1). While not relying on EDS to be quantitative in the case of carbon (and oxygen), this still indicates the possibility of the formation of a cerium-carbon compound such as CeC_2. The compact composition is generally homogenous, with only the low levels of oxygen expected from a slight amount oxidation as the sample was exposed to air during SEM loading and from a small amount of ZrO_2 from the milling media, as shown in Table 3-1.

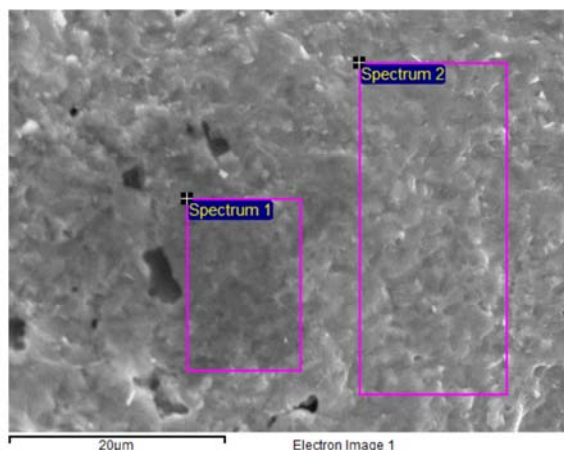Figure 30: SEM image of the cross section of a Ce_3Si_2 consolidated using PS. From this micrograph, it can be seen that the sample contains uniform grains with a few voids and minor porosity. EDS area spectra show stoichiometric Ce_3Si_2 along with impurities due to the mechanochemical synthesis process. The darker inclusion is likely a form of cerium carbide, as demonstrated in Table 3-1.

Table 3-1: Resultant elemental composition, in atomic percent (at%) of the SEM/EDS area scans shown in Figure 30. Although carbon and oxygen are not quantitative using SEM/EDS techniques, they are shown here for comparison purposes. The result of interest is that stoichiometric Ce_3Si_2 was formed.

Spectrum #	C	O	Si	Zr	Ce
Spectrum 1	66.5	7.5	8.8	1.5	14.8
Spectrum 2	25.2	10	26.7	1.9	36.2

3.1.3   Consolidation of U_3Si_2 Surrogates: Spark Plasma Sintering (SPS)

The 20 mm (inner diameter) graphite SPS die (I-85P graphite) was loaded with 4 gm of 250 μm sieved powder in a nitrogen glovebox with P_{O2} < 100 ppm. The powder was poured into the graphite die lined with graphite foil prior to cold pressing with 5 kN of force before being transferred to the SPS (Fuji Co. SPS-515S). The transfer was made in a ziplock bag to protect (to some extent) the powder from oxidation. The SPS was purged by evacuating to nearly 10 Pa and backfilling with UHP argon (repeated three times). The chamber was maintained under a vacuum of nearly 10 Pa for the sintering process and the temperature was controlled by a K-type thermocouple inserted 10 mm into the 15 mm die wall. The temperature was rapidly increased (100 $^{\circ C}/_{min}$) to a dwell temperature of 1000 °C, held there for 5 min, then quickly cooled to room temperature (100 $^{\circ C}/_{min}$). Pressure was maintained at 5 kN (15.9 MPa) throughout the sintering process, as shown in Figure 31. Sintered pellets were ground with 240 grit SiC paper to remove adhered grafoil before polishing down to 1200 grit finish. In order to record an accurate density, the surfaces of the cerium silicides must be ground to remove the carbon interaction layer from contact with the graphite foil and die. Polished Ce_3Si_2 pellets had greater than 98 %TD (as shown in Table **3-2**). A summary of all of the processed powder compositions, hold temperatures, and sintered densities is presented in

Table 3-2. The high density recorded for Ce_5Si_4 may be a result of inhomogeneity within the material (as only a portion of each pellet was measured for density) and further characterization should be performed, although it is outside the scope of this project. Additionally, Figure 32 shows the very fine microstructure of a SPS consolidated Ce_3Si_2 pellet with a few, small rounded pores appearing at grain boundaries.
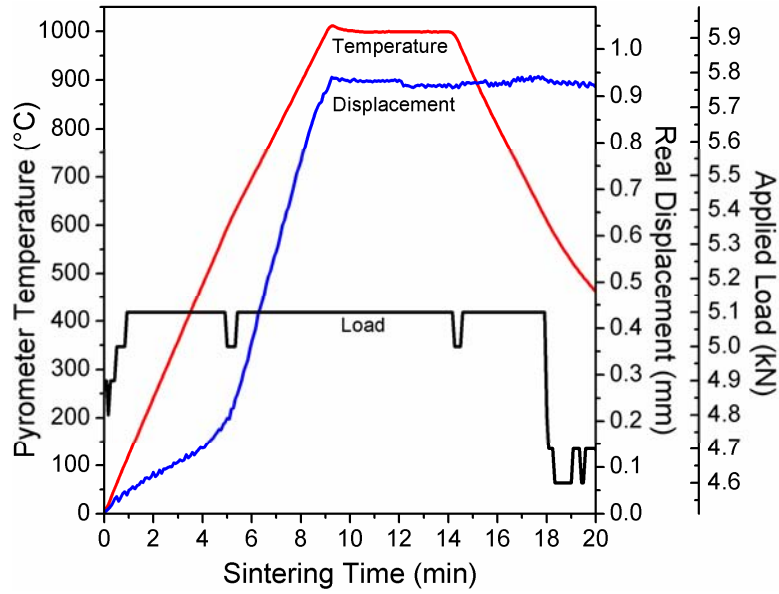
Figure 31: The applied load (black), sample temperature (red), and temperature corrected displacement (blue) during a typical SPS profile during the consolidation of Ce_3Si_2 powder. Figure adapted from Alanko, *et al.*[25].

Table 3-2: SPS processing conditions and resulting sintered cerium silicide densities.

Composition	SPS Temp. (°C)	Density	Error	% TD
Ce_5Si_3	950	5.9910	0.0146	98.5
Ce_3Si_2	1000	5.8993	0.0153	98.8
Ce_5Si_4	1125	5.8152	0.0397	101.8
CeSi	1220	5.6624	0.0736	99.0
$CeSi_{1.6}$	1150	5.2363	0.0038	99.7

Figure 32: SEM micrograph of the fracture surface of a Ce3Si2 sample consolidated using SPS at 1000 °C. A very fine microstructure is observed with a few, small rounded pores appearing at the grain boundaries. Adapted from Alanko, *et al*.[25]

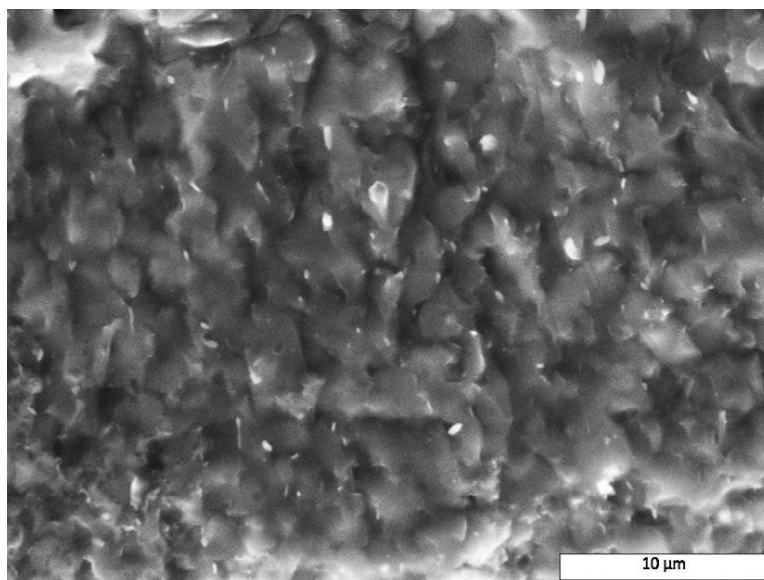### 3.1.4 *U_3Si_2 Surrogates: Oxidation Behavior*

Several samples of cerium silicides of various stoichiometries were oxidized in a Netzsch Simultaneous Thermal Analyzer (STA). Samples of approximately 40 mg were cut from SPS sintered pellets and polished flat on each face. Each polished sample was then heated at 10 $^{\circ C}/_{min}$ to 1000 °C in an atmosphere of 20% O_2, and a balance of helium.

Prior to oxidation, the Ce_3Si_2 sample was phase pure by XRD and microanalysis (as previously discussed), while the CeSi sample had some $CeSi_{1.68}$ and the $CeSi_2$ sample some free silicon. After oxidation, the Ce_3Si_2 was found to pest into a fine powder while CeSi completely oxidized but remained a coherent mass. The $CeSi_2$ sample fragmented into several roughly equal pieces. In addition to the STA measurements, a multigram sample of submicron Ce_3Si_2 powder was allowed to oxidize in air. This powder was prepared by the typical ball milling route followed by 30 minutes milling in cyclohexane and allowed to dry in vacuum before oxidation. This powder gained about 2% mass in 24 hours, as shown in Figure 34, below.

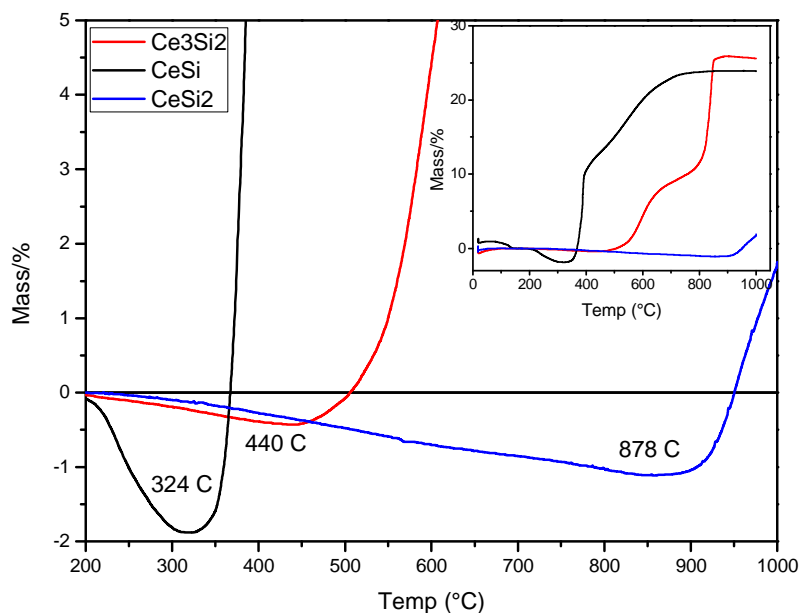Figure 33: Thermogravimetric traces showing initial oxidation studies of three cerium silicide compositions in 20% O_2 with a balance of helium. The minima for each trace is labeled. The inset shows the full data range.
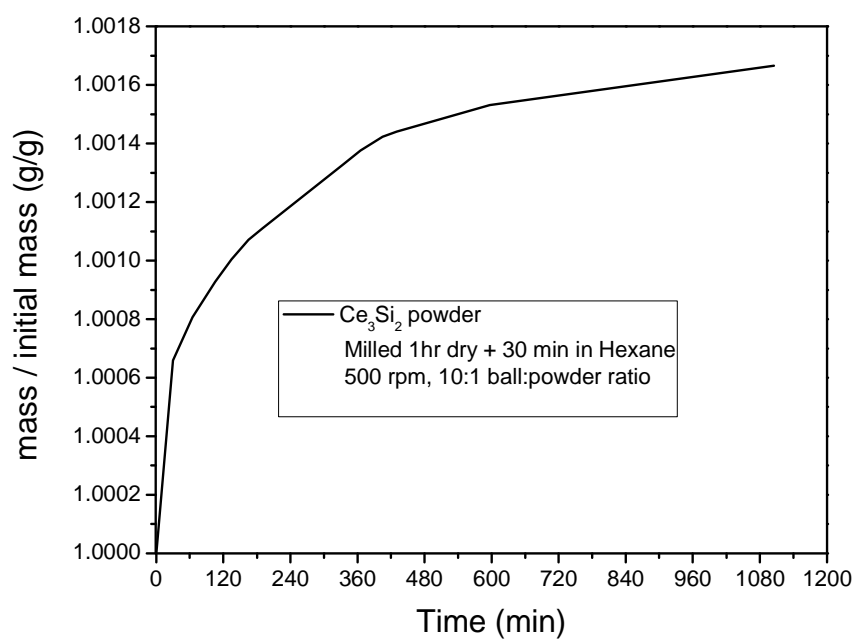

Figure 34: Plot showing the mass gain due to oxidation of a submicron Ce_3Si_2 powder in room temperature in air. There appears to be a logarithmic approach to 2% mass gain.

3.2 Radiation performance characterization of U₃Si₂ surrogates

Samples from each material type were irradiated with 2MeV protons to a fluence of 1.95×10^{18} p/cm² at 400 °C and 800 °C, and 3.9×10^{18} p/cm² at 400 °C, with a damage rate of 3.8×10^{-6} dpa/s. The irradiation resulted in the top layer ($R_p = 35$ µm) of each sample being damaged up to 0.25 and 0.51 displacements per atom (dpa), at the at implantation depth of 10µm (see Figure 35). The background pressure was about 6×10^{-6} Torr, and the irradiation temperature was monitored by two thermocouples attached diagonally to the sample holder. All five types of samples were irradiated together at a given permutation of temperature and fluence. The damage profile was simulated with the Monte Carlo simulation software "Stopping and Range of Ions in Matter" (SRIM) and calculated using the method proposed by Stoller *et al.*[27] with displacement threshold energies of Ce-$E_{th} = 25$ eV and Si-$E_{th} = 15$ eV. The 2 MeV p-irradiation yielded a long, quasi-flat damage region with a damage plateau up to 25 µm and hydrogen interstitials located beyond the depth of 30 µm (see Figure 35).
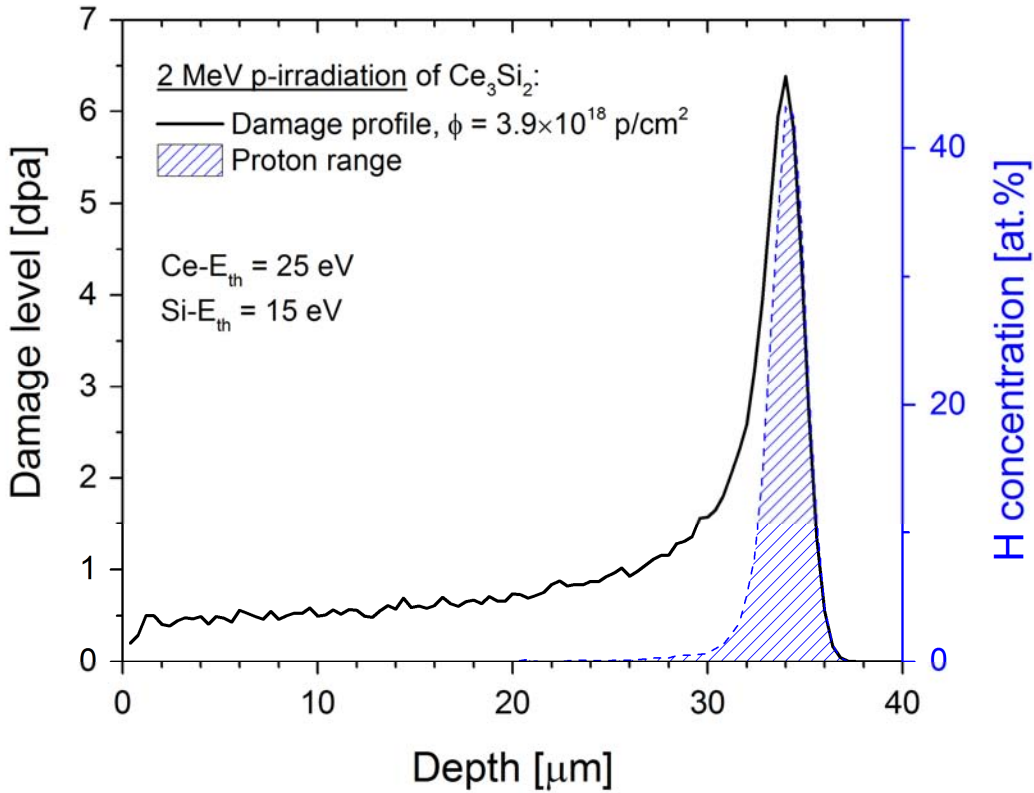
Figure 35: The SRIM damage depth profile and hydrogen concentration for 2 MeV proton-irradiated Ce₃Si₂ up to a total dose 3.9×10^{18} p/cm² (0.51 dpa at $10 µm). Irradiation results in a quasi-flat 25 µm damage profile.

Sample surfaces are characterized using scanning electron microscopy (SEM) combined with energy-dispersive X-ray spectroscopy (EDS), and the pre- and post-irradiation porosity using the front (irradiated) and the back (un-irradiated) side of each sample was analyzed with ImageJ. An SEM, model JEOL JSM-6610, was used to take surface images using secondary electron mode at 20 kV and 450x magnification. ImageJ, an image processing and analysis software, was used to calculate the surface porosity from ten

images per sample face. The porosity was computed for each image, all porosity values for the same sample were averaged, and standard deviations of these values were computed as a measure of uncertainty in the sample porosity measurements.

Sample stoichiometry, the change of microstructure, and radiation-response to ion-irradiation was monitored by XRD using Bruker D8 Discovery diffractometer in Bragg-Brentano geometry at 50 kV and 1 mA, using a Cu-Kα anode with λ = 1.54184 [Å], a 0.5mm incident slit, and a 0.5mm collimator in combination with a Montel mirror and Soller mount. The 2D Vantec 500 detector was located 200 mm from the sample. 2θ-θ scans were taken at room temperature at the range between 20º-90º with 4 steps (150 s=step) starting at 2θ = 20º and increments of 20º. Identical parameters were used for all investigated samples, and no background or K$_{\alpha 2}$ stripping was performed. The X-ray penetration depth was calculated to determine the thickness of the damage zone being investigated. The mass absorption coefficients for Ce$_3$Si$_2$ and CeSi$_2$ for the Cu-Kα radiation are 332 and 281 cm^2/g, respectively. The respective linear absorption coefficients and half value layers are therefore 1987 cm^{-1} and 3.5 µm for Ce$_3$Si$_2$, and 1504 cm^{-1} and 4.6 µm for CeSi$_2$, respectively, which means that only the damaged zone and no substrate was probed by X-rays. The experimental XRD spectra were compared with the Inorganic Crystal Structure Database, with the peak positions calculated for Cu-Kα, and Miller indices were assigned only to peaks of intensity higher than 10% I$_{max}$.

The stoichiometry of SPS-Ce$_3$Si$_2$ and SPS-CeSi$_2$ was investigated by XRD (see Figure 36). The un-irradiated SPS-CeSi2 has stoichiometry slightly inclining towards SPS-CeSi$_{1.9}$, which can be seen better at high 2θ angles. The XRD spectra have a few unidentified peaks (2θ ~ 31º, 45º, 48º) which may correspond to Si inclusions. This material (as well as all from this group) shows remarkable resistance to proton-irradiation; there is no peak shift indicating lattice constant change, the peaks preserve their intensity, which means that the long-range order is maintained, suggesting a small number of defects are present in the matrix, and there is almost no formation of new phases. SPS-Ce$_3$Si$_2$ however, shows oxidation. Proton-irradiation leads to oxide formation (see Figure 36a) and the oxide build-up depends on both irradiation temperature and damage level. All samples were irradiated together at a given temperature and damage level at a background vacuum of 6×10^{-6} Torr, yet SPS-CeSi$_2$ samples did not experience any oxidation.
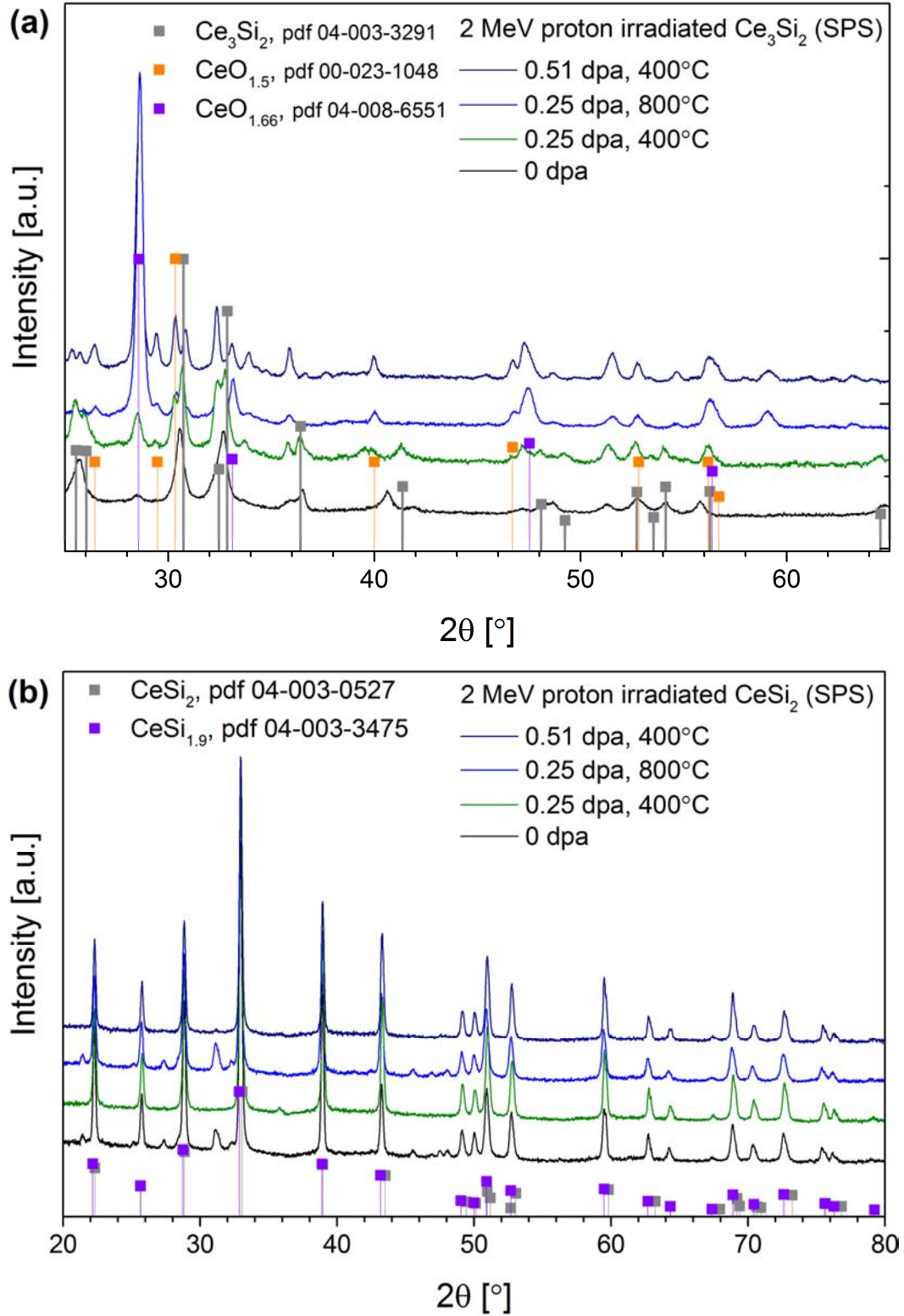
Figure 36: Stoichiometry evolution of (a) Ce_3Si_2 and (b) $CeSi_2$ for 2 MeV proton-irradiation at various temperatures and damage levels. No change is observed in $CeSi_2$; however, Ce_3Si_2 underwent oxidation.}

3.3 U₃Si₂ surrogates water corrosion

Three different compositions of cerium silicide are examined to determine their corrosion resistances. Both proton-irradiated and un-irradiated Ce_3Si_2, $CeSi_2$, and $CeSi_{1.x}$ ($x = 7$ or 9) are tested at 300 ºC and 9 MPa in an Autoclave Engineers Inc. autoclave. Tests are performed with a 3 ºC/min ramp up rate and are allowed to air cool to room temperature. 100 ml of de-ionized water is used for each test. Total elemental concentrations of Si and Ce in aqueous sample (reported in units of micrograms per liter) are determined by magnetic-sector ICP-MS (Inductively Coupled Plasma Mass Spectrometry) after digestion of the samples with a mixture of high-purity acids.

Usually, the extent of corrosion is estimated by measuring the sample mass change before and after the corrosion test, with the existing (weight loss) or removed oxide layer (metal loss). However, due to sample fracturing and the subsequent loss of some material during testing, the determined corrosion rates have limited values and not reflect the true corrosion rates of the samples. Therefore, the extent of corrosion is judged by sample stability (fracturing and cracking) as well as the thickness of the oxide layer formed during the corrosion process.

Identification of the oxide layer formed on the surface was done by XRD at parameters mentioned in Sec. 3.2. After corrosion testing, the samples were sectioned and mounted using a conductive mounting compound and a hot mounting press. The mounted samples were then polished with 1200 girt silicon carbide paper with further polishing being done with diamond paste. SEM and EDS analysis along with the sample's cross-section was done on a JEOL JSM-6610 SEM and data is used to determine the thickness of the oxide layer. Several high resolution linescans were completed on all four sides of each sample starting from the mount material, continuing through the oxide layer, and finishing in the bulk material. Elemental data was collected using an EDS detector to show the cerium silicide composition as a function of cross-sectional distance. The oxide layer thickness is found by determining where the oxygen concentration surpassed the average oxygen level in the bulk material and in the mount material. Only the thickest oxide layers found are presented in this work as oxide growth, erosion, cracking (see Figure 37) which can possibly lead to oxide spallation, are competing phenomena, and thinner oxide layers do not represent the extent of corrosion. Erosion is expected as the oxide layer grows thicker and material on the surface can be removed by circulating water.
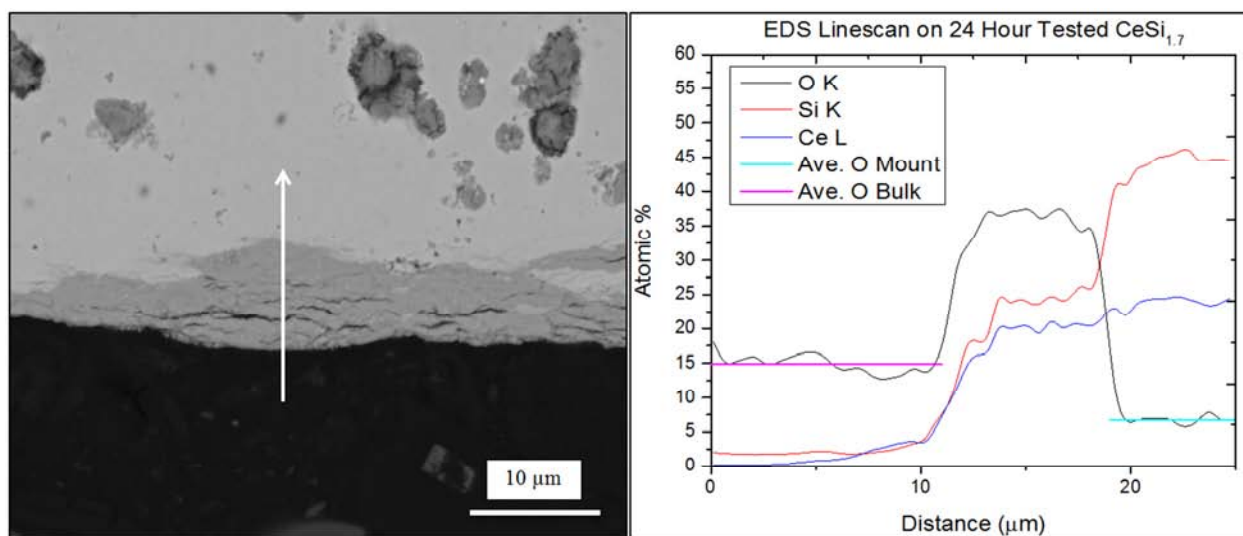
Figure 37: BSE-SEM image showing the oxide layer formed on the outer edge of the 24 hour corrosion tested CeSi$_{1.7}$ and a corresponding EDS linescan showing the oxide layer thickness.

3.3.1   Ce$_3$Si$_2$ water corrosion

Six un-irradiated Ce$_3$Si$_2$ samples are corrosion tested: two each for 1, 12, and 24 hours. Slight mass gains and positive corrosion rates are observed only in the shortest tests, while mass losses are observed in the longer tests. The mass losses are due to larger pieces that fracture off (see Figure 38) and are lost during testing. The oxide layer thickness increases with extended exposure times and reaches a maximum of 4.9 µm after 24 hours. XRD analysis (see Figure 39a) shows the evolution of the oxide layer formation with corrosion time with the oxide being identified as hexagonal cerium oxide apatite Ce$_{4.67}$(SiO$_4$)$_3$O[28] (see Figure 39b). This oxide forms through the reaction of two binary oxides CeO$_2$ and SiO$_2$. Rewriting the oxide layer composition to more closely represent the Ce$_3$Si$_2$ composition it turns into Ce$_3$Si$_{1.93}$O$_{8.35}$. From this it can be seen that there is a slight loss of silicon content and a large gain in oxygen content. Substantial oxide formation starts after 12 h water corrosion and continues such that after 24 h the oxide is thick enough that the substrate signal is no longer detected by XRD (see Figure 39b).
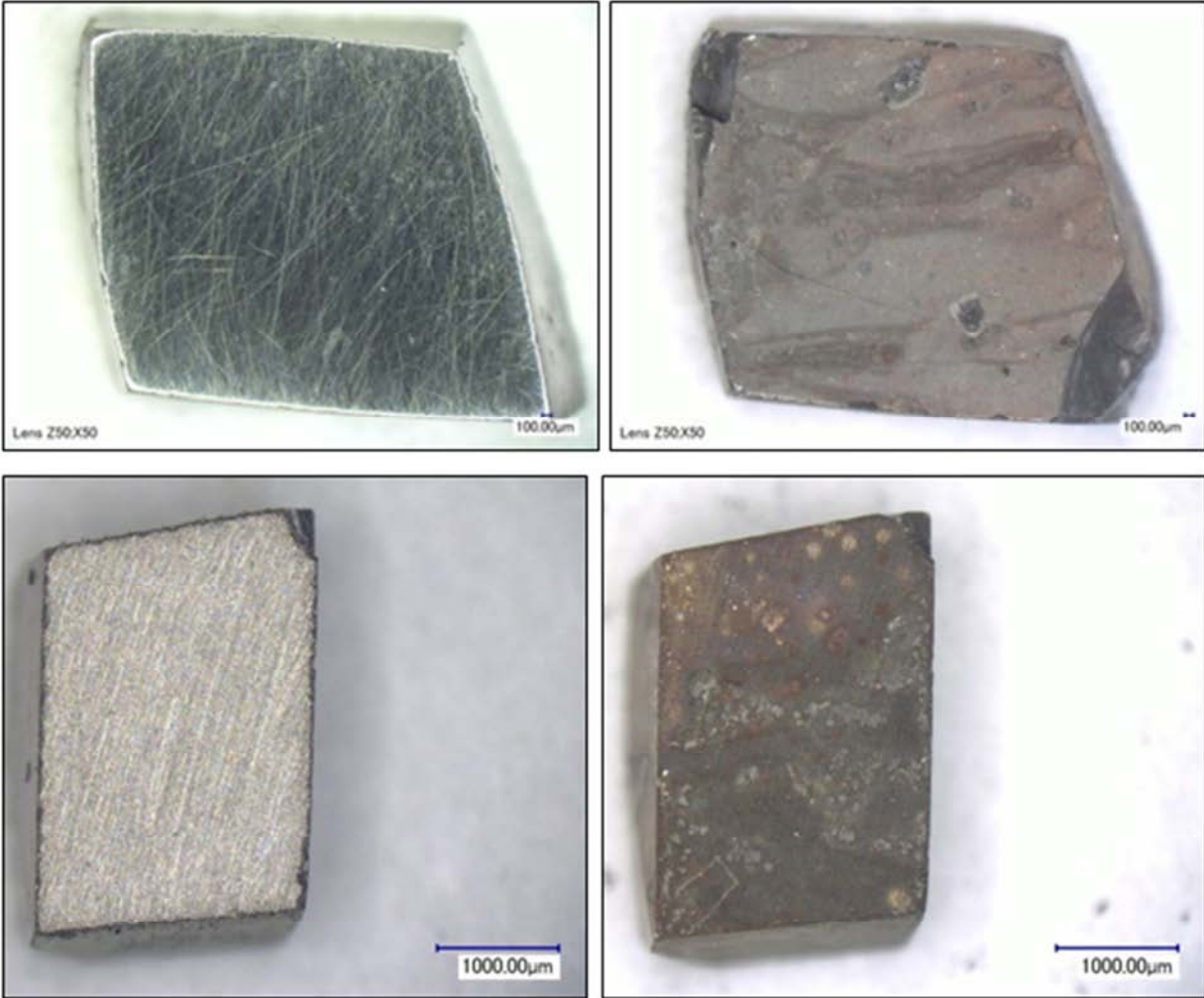
44

Figure 38: Optical images of SPS-Ce$_3$Si$_2$ (top) and SPS-CeSi$_2$ (bottom) before (left) and after (right) the water corrosion test conducted at 300 ℃ and 9 MPa for 24 hours (Ce$_3$Si$_2$) and 48 hours (CeSi$_2$). CeSi$_2$ shows higher resistance to water corrosion than Ce$_3$Si$_2$ with prolonged exposure times.
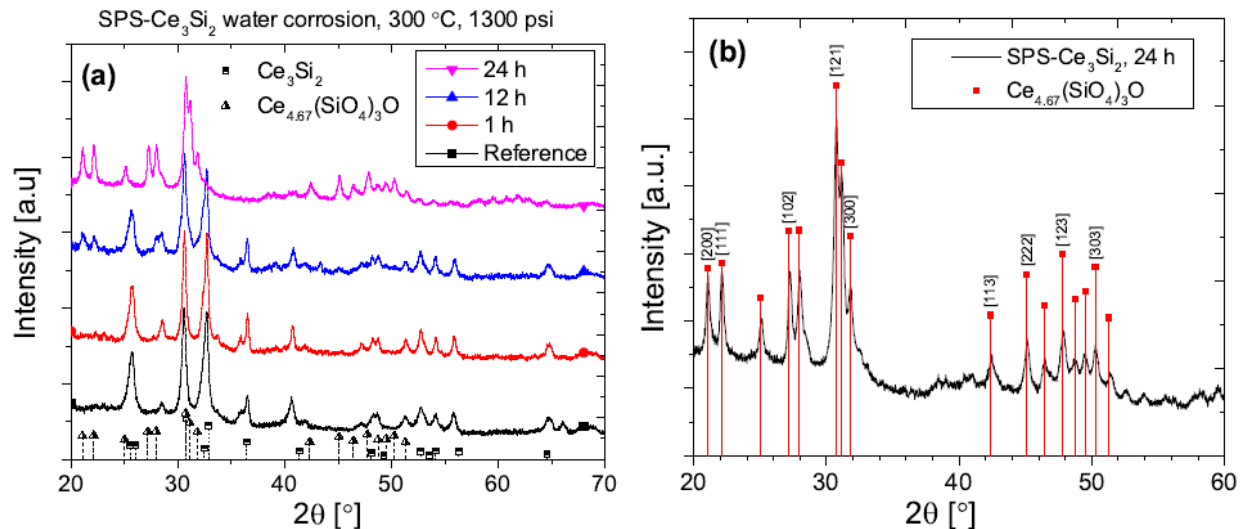
Figure 39: XRD analysis of the SPS-Ce₃Si₂ samples after water corrosion test conducted at 300 ℃, 9 MPa, for up to 24 hours. The results show the formation of $Ce_{4.67}(SiO_4)_3O$. The lack of substrate signal indicates that the oxide thickness is greater than the X-ray penetration depth of about 3.5 µm.

Two Ce_3Si_2 samples irradiated to 0.5 dpa at 800 ℃ are corroded for 12 and 24 hours. One Ce_3Si_2 sample, irradiated to 0.5 dpa at 400 ℃ is tested for 24 hours. One edge of the 12 hour 0.5 dpa at 800 ℃ sample fractures off during testing, while the 24 hour 0.5 dpa at 800 ℃ fails completely, breaking up into a fine dust with only small fragments remaining. The 24 hour 0.5 dpa at 400 ℃ sample nearly brakes in half during testing, and multiple small fractures are seen when investigating with an optical microscope. Higher temperature irradiation accelerates the fracturing process as the 400 ℃ irradiated sample would possibly break apart in a similar fashion as the 800 ℃ sample given additional exposure time. Oxide layer thicknesses for irradiated samples are thicker than un-irradiated counterparts and reach a maximum of 8.84 µm with the 0.5 dpa at 400 ℃ sample 24 hours corrosion. The thickness of the oxide layer on the 0.5 dpa at 800 ℃ sample is unable to be measured but is believed to have been thicker because of the manner in which the sample failed. No post-test XRD is performed on irradiated samples as the samples are consumed during the mounting process.

Despite increasing oxide layer growth, substantial mass losses are seen with increased exposure times in corrosion tests of Ce_3Si_2 samples. These losses occur because large pieces of the samples fracture off during testing (as-received samples) or the samples turn into dust (some irradiated specimens). This behavior is believed to be due to the brittleness of the as-received Ce_3Si_2 samples. Internal stresses coupled with the stress applied by the oxide layer may have been enough to cause the larger pieces to fracture off in a brittle fashion. Proton-irradiation increases the brittleness of the samples as irradiated Ce_3Si_2 samples performed worse than un-irradiated samples from a mechanical integrity standpoint. It happens despite the fact of higher density of implanted layers. The increased brittleness may be due to additional stresses created from the densification that occurred during irradiation resulting in an uneven stress on one surface of the sample or more likely due to the presence of post-irradiation CeO_2, which leads to faster formation of $Ce_{4.67}(SiO_4)_3O$.

Higher temperature irradiation accelerates the corrosion process as the 12 hour 800 ℃ irradiated sample has an oxide layer thicker than the 24 hour 400 ℃ irradiated sample, and the 24 hour 800 ℃ sample completely fails. The accelerated integrity failure may be due to the fact that greater densification is seen in the high temperature irradiated Ce_3Si_2 samples and it creates an even greater uneven stress on one face. The fracture pattern seen in the sample irradiated to 0.5 dpa at 400 ℃ and tested for 24 hours looks as if the sample is on its way to the same fate as the higher temperature irradiated sample.

3.3.2 *CeSi$_2$ water corrosion*

Three un-irradiated $CeSi_2$ samples are exposed for 12, 24, and 48 hours. All samples remain completely intact with only a darkening in color visible on the surface as seen in Figure 38. The oxide layer thickness for each time interval is less than that for the corresponding Ce_3Si_2 tests and it increases with the exposure time (see Figure 40). XRD analysis shows that the oxide layer formed is the same $Ce_{4.67}(SiO_4)_3O$ (or re-written as $CeSi_{0.64}O_{2.8}$) and, unlike Ce_3Si_2, the substrate signal is detected even after 48 hours test (see Figure 41a and b). XRD pattern evolution with corrosion time shows almost no signs of surface oxidation after 24 hours tests and only slight oxidation after 48 hours. This shows a slower oxide layer growth or different corrosion mechanism in $CeSi_2$ than in Ce_3Si_2 samples, and it agrees with oxide layer thickness measurements by EDS shown in Figure 40. A maximum oxide layer thickness of 3.15 µm is found 48 hours of testing.
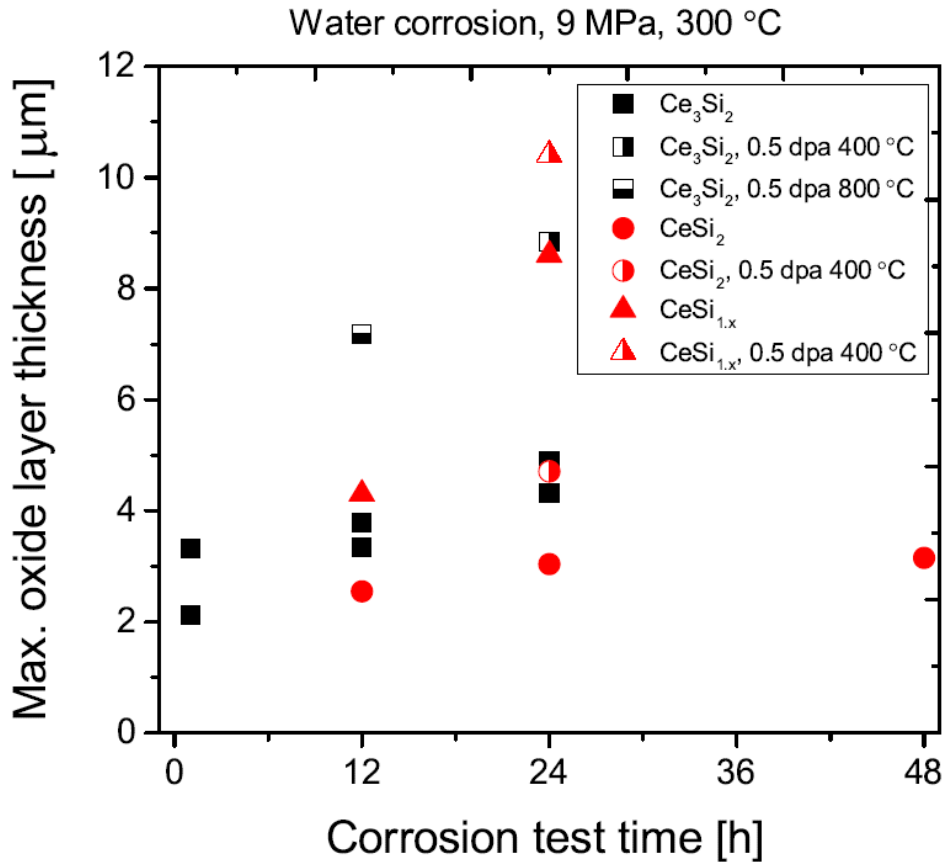

Figure 40: (a) Oxide layer thickness and (b) corrosion rate vs. corrosion time for all Ce-Si samples exposed to water at 300 ℃ and 9 MPa. Samples marked with arrows fractured during the

corrosion experiment artificially lowering the corrosion rate. $CeSi_2$ performs better than Ce_3Si_2 and proton-irradiation has accelerated the corrosion process due to oxide and defect formation.

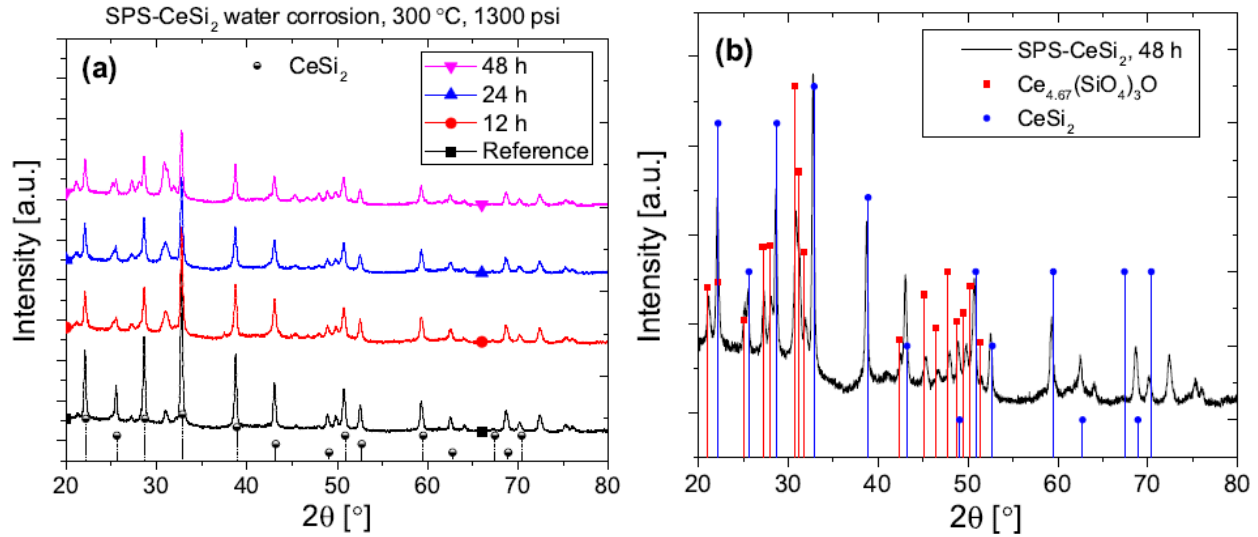

Figure 41: XRD analysis of the SPS-CeSi2 samples after water corrosion test conducted at 300 °C, 9 MPa, for up to 48 hours. The results show the formation of $Ce_{4.67}(SiO_4)_3O$ (pdf 04-008-0456). The presence of substrate signal indicates that the oxide thickness is lower than the X-ray penetration depth of about 5.44 µm.

One $CeSi_2$ sample is irradiated to 0.5 dpa at 400 °C and tested for 24 hours. This sample shows only a slight darkening of the surface and has no fractures or deformations. Surface features visible pre-test are also seen post-test. The oxide layer thickness is larger than the 24 hour un-irradiated sample with the thickest oxide layer around 4.71 µm (see Figure 40).

$CeSi_2$ samples perform better than Ce_3Si_2 samples with no fracturing or cracking and thinner oxide layer formation. This behavior is expected since oxidation studies on Ce_3Si_2 have shown that secondary particles of $CeSi_2$ form and retard further oxidation. $CeSi_2$ samples are not as brittle as Ce_3Si_2 samples and maintained integrity throughout testing. While some cerium density is being forfeited in this compound, its corrosion resistance is superior. Irradiated $CeSi_2$ performs better than Ce_3Si_2 possibly because $CeSi_2$ did not experience post-irradiation oxide formation. However, proton-irradiated $CeSi_2$ experience greater surface oxidation during water corrosion testing than its un-irradiated counterpart, which is probably caused by the presence of ion-induced defects.

3.3.3 CeSi1.x water corrosion

Two un-irradiated $CeSi_{1.x}$ samples are tested for 12 and 24 hours and one $CeSi_{1.x}$ sample irradiated to 0.5 dpa at 400 °C is tested for 24 hours. All samples remain intact with no fractures, similar to $CeSi_2$ samples. Oxide layer thickness measurement by EDS (see Figure 37) shows the formation of a thicker oxide layer for longer exposure times and its rapid growth for irradiated samples (see Figure 40). Cracks in oxide are observed (see Figure 37), which could lead to oxide spallation. XRD analysis once again shows the formation of $Ce_{4.67}(SiO_4)_3O$ oxide layer. Optical images reveal reflective flakes of what is believed to be

silicon dioxide that is not seen on other samples. Existence of this oxide is a prerequisite for the formation of $Ce_{4.67}(SiO_4)_3O$. Owing to the fact that silicon dioxide is amorphous, we are unable to confirm its presence using XRD.

Figure 40 shows measured oxide layer thicknesses against time tested. A general trend of increasing oxide thickness with increased exposure time is seen for all three compounds. In all cases irradiated samples possessed a thicker corrosion layer than un-irradiated samples.

$CeSi_{1.x}$ samples oxide layers are thicker than Ce_3Si_2 and $CeSi_2$ for both un-irradiated and irradiated samples. The integrity of the samples is comparable to that of $CeSi_2$ as no fracturing is observed. Flakes of silicon dioxide are seen on the surface. These particles appear only on the $CeSi_{1.x}$ samples and the number density of these particles increases with the corrosion time.

3.3.4   ICP-MS test results

An oxide layer of $Ce_{4.67}(SiO_4)_3O$ was formed on the surface of all tested samples. In the case of Ce_3Si_2 this means that there is a small loss of silicon and a large gain in oxygen content. For $CeSi_2$ and $CeSi_{1.x}$ there is a large loss in silicon content and a small gain in oxygen. As was confirmed by the ICP-MS test, for Ce_3Si_2 and $CeSi_2$ the excess silicon leached into water. Figure 42 shows the results of the silicon concentration measurements in the post-corrosion water. Especially for Ce_3Si_2, it can be seen that more Si leached into water (about 80-95%) than it would be expected from its stoichiometry (about 40%) if Si and Ce would erode evenly. For $CeSi_{1.9}$ the silicon concentration in the water is comparable to its content in this compound, because the excess Si did not leached into water but precipitated on the sample surface in the form of the silicon dioxide flakes.
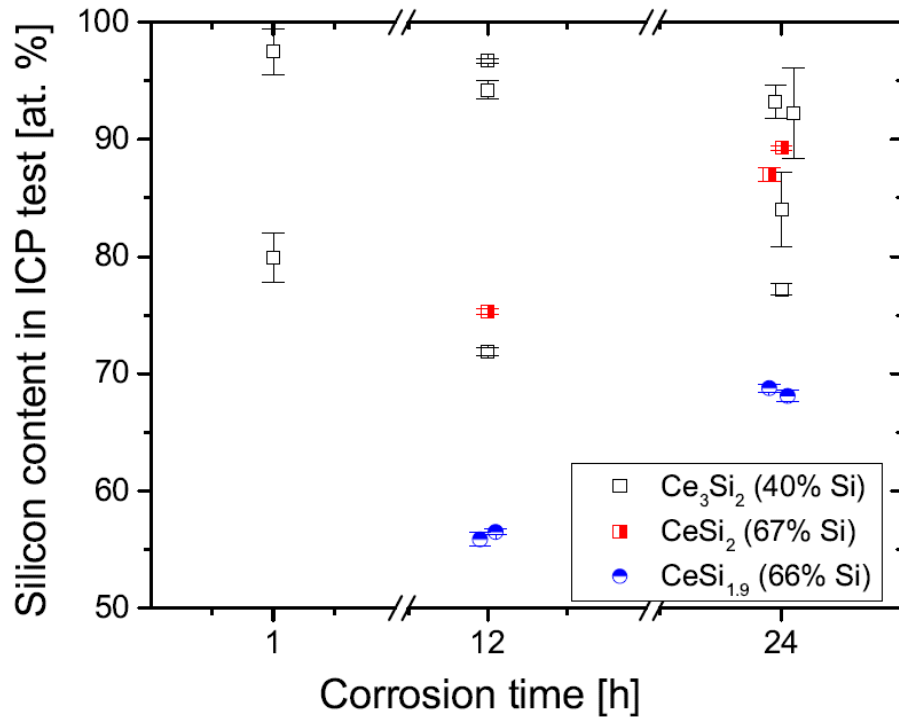

Figure 42: The silicon content (in %) in the post-corrosion water for Ce_3Si_2, $CeSi_2$, and $CeSi_{1.9}$ samples. No distinction is made between as-received and irradiated samples.

3.4 Thermal conductivity of U$_3$Si$_2$ surrogates

Thermal conductivity was measured using modulated thermo-reflectance microscopy (MTRM). MTRM is a pump-probe method that images thermal waves excited by an amplitude-modulated beam and is best suited for measuring the thermal properties of thin films. Following the irradiation and prior to the measurements, the cerium silicide samples were coated with a ≈60 nm thick aluminum metal transducer layer using magnetron sputtering. The aluminum layer insures optical absorption of the pump at the surface and acts as a sensor for temperature changes based on temperature dependence of the reflectivity. The technique utilizes amplitude modulation of the pump at various frequencies ranging from 1 kHz to 100 kHz to confine the thermal wave to appropriate depths. High frequency profiles have the best signal-to-noise ratio but also poor sensitivity to conductivity of unknown material. On the other hand, low-frequency waves penetrate deeper into the substrate but have poor signal-to-noise ratio and, more pertinent to this work, would be affected by the peak damage zone of ion-irradiated samples. Here, an optimal frequency range most sensitive to the plateau damage region in the irradiated sample was chosen. The pump beam heats the surface of the sample, and the probe beam measures the resulting temperature change through the change of optical reflectivity. Both beams are focused on the sample using a 50x microscope objective resulting in ≈1 µm spot sizes. A phase lag between the heat source and the thermal wave at a single point is measured as a function of distance between the pump and probe. The slope of the thermal profile is related to the thermal properties of the metal and substrate.

The transducer Al film introduces a number of additional parameters, such as film thickness and thermal resistance. To reduce the number of unknown thermal properties of the substrate, an additional step was performed: the aluminum layer was also deposited on a microscope slide with known thermal properties. The thermal conductivity of the Al film was measured using this microscope slide standard. The uncertainty of the measurement was determined by the quality of the data (signal-to-noise) and the sensitivity of the thermal wave to the substrate's thermal properties for a given frequency.

The thermal conductivity was determined from the fitting of measured thermal wave profiles, with specific heat C_p and density values being known. Specific heat values were theoretically calculated using the DuLong-Petit law and assumed to be the same for un-damaged and damaged samples. The specific heat was calculated to be 0.2812 J/(gK) and 0.4095 J/(gK) for Ce$_3$Si$_2$ and CeSi$_2$, respectively.

The values of thermal diffusivity obtained from MTRM depends on the fabrication method – the values obtained are 4×10^{-6} m^2/s for the reference PS-Ce$_3$Si$_{2+0.1}$ samples, 5.7×10^{-6} m^2/s for SPS-Ce$_3$Si$_2$ and 6.5×10^{-6} m^2/s for SPS-CeSi$_{2\pm0.1}$. In almost all cases, the thermal diffusivity decreased by 25%-50%, with the reduction being dependent on the increasing damage level and not the irradiation temperature.

The thermal conductivity results, normalized to 95% theoretical density for all materials, are summarized in Figure 43. After normalization, the thermal conductivity of Ce$_3$Si$_2$ samples is about 9 W/(mK), independent of the fabrication method, which is comparable with the value reported by Shimizu[29] and White *et al.*[30] for U$_3$Si$_2$ suggesting that Ce$_3$Si$_2$ is a good surrogate for its radioactive counterpart. Reference CeSi$_2$ and Ce$_3$Si$_{1.9}$ materials show much higher thermal conductivities above 14.5 W/(mK). Most of the samples with a lower silicon content (Ce$_3$Si$_{2+0.1}$) experience sharp reduction in thermal

conductivity after proton-irradiation, while the $CeSi_2$ and $Ce_3Si_{1.9}$ specimens recorded much smaller change (see Figure 44). This response is connected to the oxidation of $Ce_3Si_{2+0.1}$ under ion-irradiation and to the inclusion of the CeO_{1+x} phase which has lower thermal conductivity.

The irradiation performance of uranium silicide surrogates and UO_2[31] in terms of thermal conductivity is compared in Figure 44. The damage level values for 2 MeV Ar-irradiated UO_2 were calculated in the same manner as for cerium silicide, assuming the threshold displacement energies of U and O being 20 eV. Presented thermal conductivity values are calculated for 95% TD. At 0 dpa the thermal conductivity of UO_2, Ce_3Si_2, and U_3Si_2 from Shimizu[29] and White *et al.*[30] have a comparable λ of about 9 W/(mK), which quickly decays with damage level to half of its value at 0.51 dpa. This result suggests no advantage of U_3Si_2 over UO_2 in terms of initial thermal conductivity or radiation resistance at low temperatures and is caused by the surrogate oxidation. $CeSi_2$, however, shows much higher initial thermal conductivity and better resistance to irradiation. The results presented here indicate that thermal conductivity studies of U_3Si_2 at high temperature are necessary to ascertain whether it can retain its intermetallic behavior in the presence of radiation-induced defects.
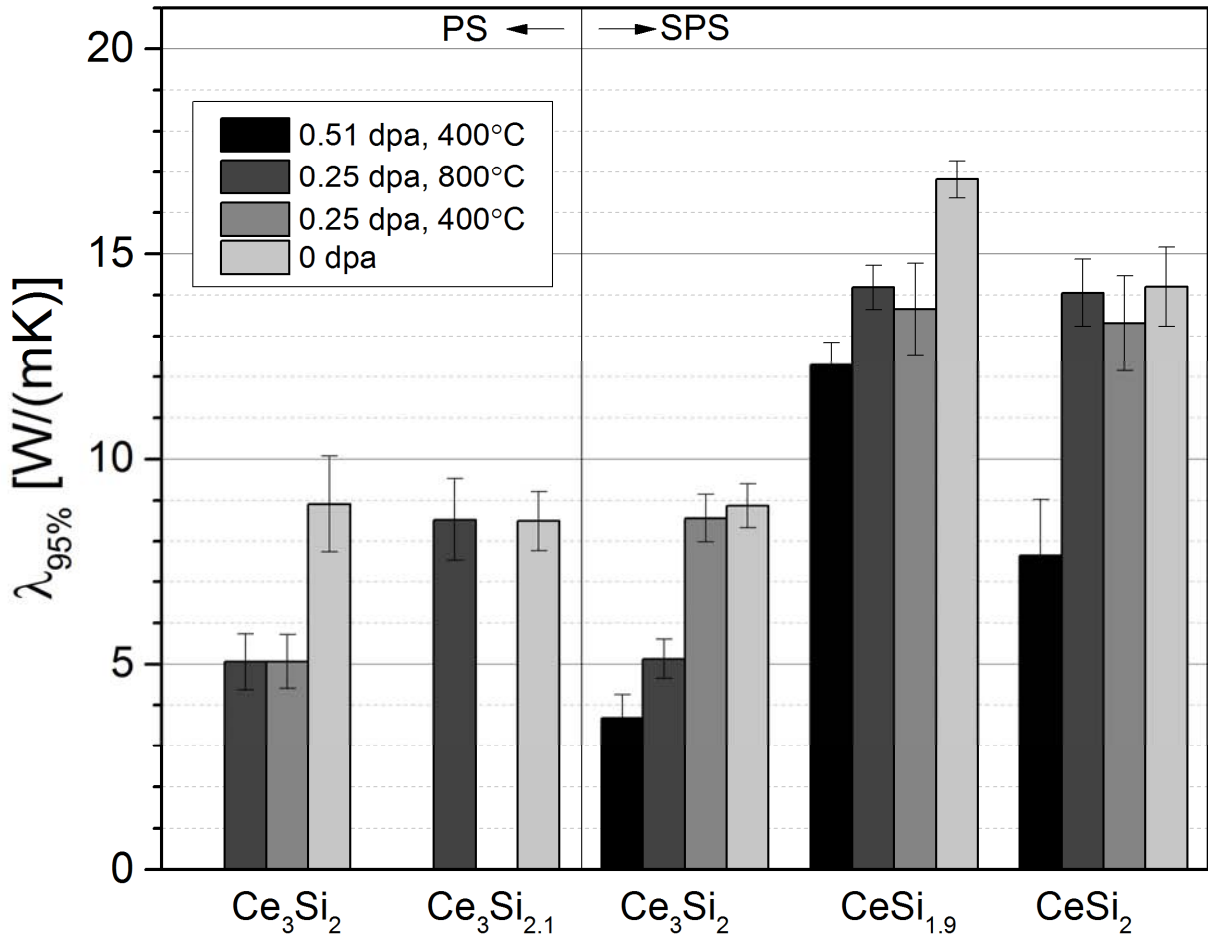

Figure 43: Thermal conductivity values for all cerium silicide materials, normalized to 95% theoretical density. $CeSi_{2-x}$ specimens show higher thermal conductivity values and superior irradiation performance.
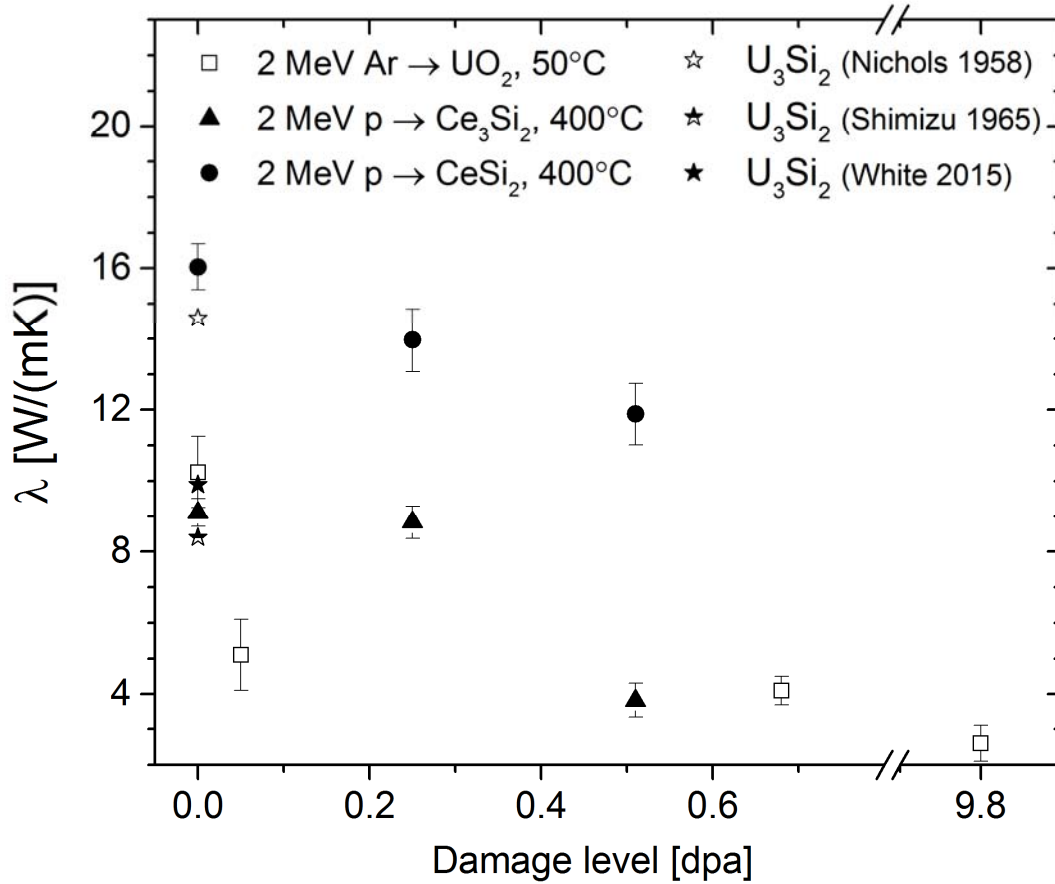
Figure 44: Comparison of thermal conductivity values (normalized to 95% theoretical density) for un-irradiated U_3Si_2[29, 30, 32] and 2 MeV proton- and argon-[31] irradiated cerium silicide and uranium dioxide specimens. Irradiated UO_2 shows a sharp decrease in thermal conductivity under small doses, while irradiated SPS $CeSi_{2-x}$ materials perform better below 0.51 dpa.

In the proton-irradiated samples, a gradual decrease in thermal conductivity upon irradiation at 400 °C in all irradiated samples is observed, which is attributed to accumulation of radiation-induced defects. These defects act as scattering centers, affecting the ability of lattice vibrations and electrons to move and thus efficiently conduct heat. One notable observation is that $Ce_3Si_{2.1}$ and $Ce_3Si_{1.9}$ experience less reduction in thermal conductivity. This result can be attributed to the difference in relative contribution of lattice and electronic conductivities and how these heat conduction processes are affected by radiation damage. As mentioned earlier, lattice thermal conductivity is significantly affected by the radiation damage due to defects, whereas electronic conductivity is expected to be affected to a much smaller extent. The experimental values are in agreement with this fact: the thermal conductivities of $Ce_3Si_{2.1}$ and $Ce_3Si_{1.9}$, having strong electronic contributions, exhibit much smaller reductions compared to their stoichiometric counterparts.

An alternative reason for a smaller conductivity reduction in non-stoichiometric samples may be the enhanced mobility of defects under irradiation in these materials. Defects that are present to accommodate non-stoichiometry typically enhance mobility of defects overall, leading to improved radiation tolerance. Under this mechanism, the smaller reduction of conductivity is merely a result of reduced defect concentration after irradiation in non-stoichiometric samples. Presently available information obtained from microstructure characterization is not adequate to make a conclusion on which mechanism prevails. Enhanced mobility of defects at higher temperatures is evidenced by smaller conductivity reduction in samples irradiated at 800 ℃. The fact that the samples irradiated to 0.25 dpa at 800 ℃ exhibit smaller conductivity reduction compared to those at 800 ℃ is indicative of annealing affects. At higher temperatures defects are more mobile and can anneal out which has a strong impact on thermal conductivity.

References

1. R. B. Matthews, K. M. Chidester, C. W. Hoth, R. E. Mason, and R. L. Petty, "Fabrication and testing of uranium nitride fuel for space power reactors," *Journal of Nuclear Materials,* 151[3] 334 (1988).
2. T. Muromura and H. Tagawa, "Formation of uranium mononitride by reaction of uranium-dioxide with carbon in ammonia and a mixture of hydrogen and nitrogen. 1. Synthesis of high-purity UN," *Journal of Nuclear Materials,* 71[1] 65-72 (1977).
3. V. G. Baranov, A. V. Tenishev, R. S. Kuzmin, S. A. Pokrovskiy, V. V. Mikhalchik, V. A. Astafyev, M. L. Taubin, and E. S. Solntseva, "Thermal stability investigation technique for uranium nitride," *Ann. Nucl. Energy,* 87, Part 2 784-92 (2016).
4. J. Bugl and A. A. Bauer, "Corrosion and oxidation characteristics of uranium mononitride." in International symposium on compounds of interest in nuclear reactor technology, Vol. X. Edited by J. T. Waber, P. Chiotti, and W. N. Miner. Nuclear Metallurgy, Ann Arbor, MI, 1964.
5. J. E. Antill and B. L. Myatt, "Kinetics of oxidation of UN and U(CO) in carbon dioxide steam and water at elevated temperatures," *Corros Sci,* 6[1] 17-23 (1966).
6. R. M. Dell, V. J. Wheeler, and N. J. Bridger, "Hydrolysis of uranium mononitride," *Transactions of the Faraday Society,* 63[533P] 1286-94 (1967).
7. V. J. Tennery and E. S. Bomar, "Sintering of (U,Pu)N as a function of Temperature and Nitrogen Pressure," *Transactions of the American Nuclear Society,* 19 101-02 (1974).
8. V. J. Tennery, T. G. Godfrey, and R. A. Potter, "Sintering of U N as a function of temperature and N2 pressure," *Journal of the American Ceramic Society,* 54[7] 327-31 (1971).
9. H. Matzke, "Atomic mechanisms of mass transport in ceramic nuclear fuel materials," *Journal of the Chemical Society Faraday Transactions,* 86[8] 1243-56 (1990).
10. H. Inouye and J. M. Leitnake, "Equilibrium nitrogen pressures and thermodynamic properties of UN," *Journal of the American Ceramic Society,* 51[1] 6 (1968).
11. A. A. Bauer, "Nitride Fuels: Properties and Potentials," *Reactor Technology,* 15[2] 87-104 (1972).
12. J. M. Cleveland, G. H. Bryan, C. R. Heiple, and R. J. Sironen, "A new, low-temperature synthesis of plutonium and uranium nitrides," *Nucl. Technol.,* 25[3] 541-5 (1975).
13. H. Matzke, "Science of Advanced LMFBR Fuels," pp. 740. Elsevier Science Publishing Company, Inc.: Amsterdam, The Netherlands, (1986).
14. N. H. Olschewski, J.-P. Glatz, H. Bokelund, and M. J.-F. Leroy, "Fate of nitrogen upon reprocessing of nitride fuels," *Journal of Nuclear Materials,* 188 244-48 (1992).
15. N. Oi, S. Hirayama, I. Tanabe, A. Muramatsu, and T. Kawada, "Preparation of high density uranium nitride and uranium carbonitride fuel pellets," *Journal of Nuclear Science and Technology,* 9[9] 521-7 (1972).
16. M. Paljevic and Z. Despotovic, "Oxidation of Uranium Nitride," *Journal of Nuclear Materials,* 57[3] 253-57 (1975).
17. W. D. Wilkinson, "Uranium Metallurgy: Uranium Process Metallurgy," Vol. 1. Interscience Publishers: New York, (1962).
18. P. Malkki, M. Jolkkonen, T. Hollmer, and J. Wallenius, "Manufacture of fully dense uranium nitride pellets using hydride derived powders with spark plasma sintering," *Journal of Nuclear Materials,* 452[1-3] 548-51 (2014).
19. B. J. Jaques, J. Watkins, J. R. Croteau, G. A. Alanko, B. Tyburska-Pueschel, M. Meyer, P. Xu, E. J. Lahoda, and D. P. Butt, "Synthesis and sintering of UN-UO2 fuel composites," *Journal of Nuclear Materials,* 466 745-54 (2015).

20. K. Iakoubovskii, K. Mitsuishi, Y. Nakayama, and K. Furuya, "Thickness measurements with electron energy loss spectroscopy," *Microscopy Research and Technique,* 71[8] 626-31 (2008).

21. K. Urso, "Corrosion studies of cerium silicides as surrogates for uranium silicides." in*,* Vol. MSMSE. University of Wisconsin-Madison, 2014.

22. S. Sugihara and S. Imoto, "Hydrolysis of uranium nitrides," *J Nucl Sci Technol-T,* 6[5] 237 (1969).

23. M. V. Bulanova, P. N. Zheltov, K. A. Meleshevich, P. A. Saltykov, and G. Effenberg, "Cerium-silicon system," *Journal of Alloys and Compounds,* 345[1-2] 110-15 (2002).

24. A. Berche, C. Rado, O. Rapaud, C. Gueneau, and J. Rogez, "Thermodynamic study of the U-Si system," *Journal of Nuclear Materials,* 389[1] 101-07 (2009).

25. G. A. Alanko, B. Jaques, A. Bateman, and D. P. Butt, "Mechanochemical synthesis and spark plasma sintering of the cerium silicides," *Journal of Alloys and Compounds,* 616 306-11 (2014).

26. B. J. Jaques, D. D. Osterberg, G. A. Alanko, S. Tamrakar, C. R. Smith, M. F. Hurley, and D. P. Butt, "In situ characterization of the nitridation of dysprosium during mechanochemical processing," *Journal of Alloys and Compounds,* 619 253-61 (2015).

27. R. E. Stoller, M. B. Toloczko, G. S. Was, A. G. Certain, S. Dwaraknath, and F. A. Garner, "On the use of SRIM for computing radiation damage exposure," *Nuclear Instruments and Methods in Physics Research Section B: Beam Interactions with Materials and Atoms,* 310 75-80 (2013).

28. A. C. Tas and M. Akinc, "Cerium Oxygen Apatite (Ce4.67[SiO4]3O) X-Ray Diffraction Pattern Revisited," *Powder Diffraction,* 7[04] 219-22 (1992).

29. H. Shimizu, "The properties and irradiation behavior of U3Si2." in Atomics International. 1965.

30. J. T. White, A. T. Nelson, J. T. Dunwoody, D. D. Byler, D. J. Safarik, and K. J. McClellan, "Thermophysical properties of to 1773 K," *Journal of Nuclear Materials,* 464 275-80 (2015).

31. P. B. Weisensee, J. P. Feser, and D. G. Cahill, "Effect of ion irradiation on the thermal conductivity of UO2 and U3O8 epitaxial layers," *Journal of Nuclear Materials,* 443[1–3] 212-17 (2013).

32. R. W. Nichols, "Ceramic fuels - properties and technology," *Nucl. Eng.,* 3[324] (1958).

4 Publications

4.1 Dissertations

- T.J. Eiden, "Radiation performance of uranium mononitride and cerium silicide", Master's Thesis, University of Wisconsin-Madison (2013)

- G. A. Alanko, "Thermodynamics and Reaction Kinetics during Mechanochemical Synthesis and Environmental Testing of Lanthanide and Actinide Refractory Materials." (2014). Doctoral Dissertation. Boise State University Theses and Dissertations. Paper 851.

- A.R. Reinicke, "Thermal conductivity of cerium silicide as surrogate for uranium silicide fuels", Master Dissertation, University of Wisconsin-Madison (2014)

- K.J. Urso, "Corrosion studies of cerium silicides as surrogates for uranium silicides", Master's Thesis, University of Wisconsin-Madison (2014)

- B.J. Jaques, "Reaction Kinetics of Rare Earth and Actinide Materials." (2015). Doctoral Dissertation. Boise State University Theses and Dissertations. Paper 928.

4.2 Peer-review articles

- B.J. Jaques, J. Watkins, J.R. Croteau, G.A. Alanko, B. Tyburska-Püschel, M. Meyer, P. Xu, E.J. Lahoda, and D.P. Butt, "Synthesis and Sintering of UN-UO$_2$ Fuel Composites." Journal of Nuclear Materials, 466 745-754 (2015)

- G. A. Alanko, B. J. Jaques, A. Bateman, and D. P. Butt, "Mechanochemical synthesis and spark plasma sintering of the cerium silicides," *Journal of Alloys and Compounds*, 616 306-311 (2014)

- G. A. Alanko and D. P. Butt, "Mechanochemical synthesis of uranium sesquisilicide," Journal of Nuclear Materials, 451[1-3] 243-248 (2014)

- A.R. Reinicke, M. Khafizov, K. Sridharan, B.J. Jaques, G. Alanko, M. Meyer, P. Xu, D.P. Butt, B. Tyburska-Pueschel, "Densification and thermal conductivity of proton-irradiated cerium silicide", in preparartion.

- K.J. Urso, K. Sridharan, B.J. Jaques, G. Alanko, D.P. Butt, M. Meyer, P. Xu, , B. Tyburska-Pueschel, "High Temperature Corrosion Testing of Uranium Silicide Surrogates", accepted for publication in Nuclear Technology.

- L. He, B. Tyburska-Püschel, K. Sridharan, M. Meyer, B.J. Jaques, G. Alanko, D.P. Butt, P. Xu, "Comparison of the microstructure of the proton-irradiated UN and UO$_2$", in preparation.

4.3 Presentations

- B.J. Jaques and D.P. Butt, "Synthesis of accident tolerant nitride fuels." Presented at Global 2015: Nuclear Fuel Cycle for a Low Carbon Future, Paris, France. September 21-24, 2015

- D.P. Butt and B.J. Jaques, "Research activities in synthesis and performance of uranium nitride-based nuclear (composite) fuels." Presented at the 3rd annual CARAT meeting, Hopkins, SC, July 13, 2015.

- B.J. Jaques, G.A. Alanko, P. Xu, E.J. Lahoda, and D.P. Butt, "Synthesis of advanced multiphase actinide fuels." Presented at the Materials Science and Technology 2014 Conference, Pittsburgh, PA, October 12-16, 2014. Invited.

- B.J. Jaques, G. A. Alanko, P. Xu, E. J. Lahoda, and D. P. Butt, "Synthesis of advanced multiphase actinide fuels." Presented at the Materials Science and Technology 2014 Conference, Pittsburgh, PA, October 12-16, 2014. Invited.

- G.A. Alanko, B.J. Jaques, and D.P. Butt, "Synthesis of U_3Si_2 by high energy ball milling." Presented at the 143rd annual TMS 2014 Conference, San Diego, CA, February 16-20, 2014.

- A. Bateman, G.A. Alanko, B.J. Jaques, and D.P. Butt, "Novel fabrication techniques for cerium silicide as a surrogate nuclear fuel." Presented at the 10th annual Boise State University Undergraduate Research Conference, Boise, ID, April 15, 2013

Degrees Awarded

Thomas Eiden, M.Sc. 2013

Gordon Alanko, Ph.D. 2014

Adam Reinicke, M.Sc. 2014

Kolton Urso, M.Sc. 2014

Brian Jaques, Ph.D. 2015